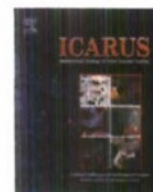
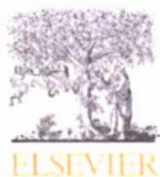


DTIC COPY

REPORT DOCUMENTATION PAGE				Form Approved OMB No. 0704-01-0188	
<small>The public reporting burden for this collection of information is estimated to average 1 hour per response, including the time for reviewing instructions, searching existing data sources, gathering and maintaining the data needed, and completing and reviewing the collection of information. Send comments regarding this burden estimate or any other aspect of this collection of information, including suggestions for reducing the burden to Department of Defense, Washington Headquarters Services, Directorate for Information Operations and Reports (0704-0188), 1215 Jefferson Davis Highway, Suite 1204, Arlington VA 22202-4302. Respondents should be aware that notwithstanding any other provision of law, no person shall be subject to any penalty for failing to comply with a collection of information if it does not display a currently valid OMB control number.</small>					
<b>PLEASE DO NOT RETURN YOUR FORM TO THE ABOVE ADDRESS.</b>					
<b>1. REPORT DATE (DD-MM-YYYY)</b> 10-11-2010		<b>2. REPORT TYPE</b> Reprint		<b>3. DATES COVERED (From - To)</b>	
<b>4. TITLE AND SUBTITLE</b> Calibration against the Moon I: A disk-resolved lunar model for absolute reflectance calibration				<b>5a. CONTRACT NUMBER</b>	
				<b>5b. GRANT NUMBER</b>	
				<b>5c. PROGRAM ELEMENT NUMBER</b> 62601F	
<b>6. AUTHORS</b> Edward J. Kennelly* Stephan D. Price Kathleen E. Kraemer Ryan Aschbrenner*				<b>5d. PROJECT NUMBER</b> 1010	
				<b>5e. TASK NUMBER</b> SB	
				<b>5f. WORK UNIT NUMBER</b> ZZ	
<b>7. PERFORMING ORGANIZATION NAME(S) AND ADDRESS(ES)</b> Air Force Research Laboratory /RVBYB 29 Randolph Road Hanscom AFB, MA 01731-3010				<b>8. PERFORMING ORGANIZATION REPORT NUMBER</b> AFRL-RV-HA-TR-2010-1137	
<b>9. SPONSORING/MONITORING AGENCY NAME(S) AND ADDRESS(ES)</b>				<b>10. SPONSOR/MONITOR'S ACRONYM(S)</b> AFRL/RVBYB	
				<b>11. SPONSOR/MONITOR'S REPORT NUMBER(S)</b>	
<b>12. DISTRIBUTION/AVAILABILITY STATEMENT</b> Approved for Public Release; distribution unlimited.					
<b>13. SUPPLEMENTARY NOTES</b> *AER, Inc., 131 Hartwell Ave., Lexington, MA 02421 Reprinted from <i>Icarus</i> , 210 (2010) 14-36. © 2010 Elsevier, B. V.					
<b>14. ABSTRACT</b> We present a model of the absolute radiance of the disk-resolved Moon at visible to near infrared wavelengths. It has been developed in order to use the Moon as a calibration reference, particularly by space-based sensors observing the Earth. We begin with the development of Hillier et al. (Hillier, J., Buratti, B., Hill, K.[1999]. <i>Icarus</i> 141, 205-225) for the reflectance as a function of phase angle and base the lunar reflectance on the Clementine 0.750 $\mu$ m basemap. We adopt Hapke's (Hapke, B. [2002]. <i>Icarus</i> 157, 523-534) expression for the multiple scattering term, including the more accurate approximation to the Chandrasekhar H function. The geometry is based on the Jet Propulsion Laboratory Lunar Ephemeris DE421, and the topographic slope is from the Kaguya-LALT laser altimetry (Araki, H., and 10 colleagues [2009]. <i>Science</i> 323, 897-900). We define three types of terrain by combining the reflectance from the Clementine basemap and the topographic model to specify maria, highlands, and crater regions, and allow mixed types between each class. Parameters of the model are solved for as a function of surface type and wavelength by comparison against data "chips" from the Robotic Lunar Observatory (ROLO; Kieffer, H. H., Stone, T. C. [2005]. <i>Astron J.</i> 129, 2887-2901). The reflectance in any waveband maybe computed by spectral interpolation of the model predictions relative to the scaled Apollo 16 soil spectrum. The accuracy of the model, evaluated against ROLO imagery, was found to be 2-4%.					
<b>15. SUBJECT TERMS</b> Moon, surface					
<b>16. SECURITY CLASSIFICATION OF:</b>			<b>17. LIMITATION OF ABSTRACT</b>	<b>18. NUMBER OF PAGES</b>	<b>19a. NAME OF RESPONSIBLE PERSON</b> Kathleen E. Kraemer
<b>a. REPORT</b>  UNCL	<b>b. ABSTRACT</b>  UNCL	<b>c. THIS PAGE</b>  UNCL			<b>19b. TELEPHONE NUMBER (Include area code)</b>



## Calibration against the Moon

### I: A disk-resolved lunar model for absolute reflectance calibration

Edward J. Kennelly<sup>a</sup>, Stephan D. Price<sup>b</sup>, Kathleen E. Kraemer<sup>b,\*</sup>, Ryan Aschbrenner<sup>a</sup>

<sup>a</sup> Atmospheric and Environmental Research, Inc., 131 Hortwell Avenue, Lexington, MA 02421, United States

<sup>b</sup> Air Force Research Laboratory, Space Vehicles Division, 29 Randolph Road, Hanscom AFB, MA 01731, United States

#### ARTICLE INFO

##### Article history:

Received 18 December 2009

Revised 7 May 2010

Accepted 27 May 2010

Available online 4 June 2010

##### Keyword:

Moon, Surface

#### ABSTRACT

We present a model of the absolute radiance of the disk-resolved Moon at visible to near infrared wavelengths. It has been developed in order to use the Moon as a calibration reference, particularly by space-based sensors observing the Earth. We begin with the development of Hillier et al. (Hillier, J., Buratti, B., Hill, K. [1999]. *Icarus* 141, 205–225) for the reflectance as a function of phase angle and base the lunar reflectance on the Clementine 0.750  $\mu\text{m}$  basemap. We adopt Hapke's (Hapke, B. [2002]. *Icarus* 157, 523–534) expression for the multiple scattering term, including the more accurate approximation to the Chandrasekhar H function. The geometry is based on the Jet Propulsion Laboratory Lunar Ephemeris DE 421, and the topographic slope is from the Kaguya-LALT laser altimetry (Araki, H., and 10 colleagues [2009]. *Science* 323, 897–900). We define three types of terrain by combining the reflectance from the Clementine basemap and the topographic model to specify maria, highlands, and crater regions, and allow mixed types between each class. Parameters of the model are solved for as a function of surface type and wavelength by comparison against data "chips" from the Robotic Lunar Observatory (ROLO; Kieffer, H.H., Stone, T.C. [2005]. *Astron. J.* 129, 2887–2901). The reflectance in any waveband may be computed by spectral interpolation of the model predictions relative to the scaled Apollo 16 soil spectrum. The accuracy of the model, evaluated against ROLO imagery, was found to be 2–4%.

© 2010 Elsevier Inc. All rights reserved.

#### 1. Introduction

In the late 1990s, Kieffer, Stone, and colleagues at the US Geological Survey (USGS) set out to establish the Moon as a calibration reference for space-based sensors looking at the Earth. Kieffer and Wildey (1996) defined the measurements and modeling required for this task. The USGS then began an observing program with the Robotic Lunar Observatory (ROLO), which consists of two 20 cm telescopes co-aligned on the same telescope mount; one instrument images the Moon in 23 narrow visible spectral bands between 0.350 and 0.950  $\mu\text{m}$  onto a  $512 \times 512$  element CCD with 4" pixels while the other telescope images the Moon in nine narrow near-infrared bands between 0.95 and 2.45  $\mu\text{m}$  onto a  $256 \times 256$  array with  $\sim 8$ " pixels. Kieffer and Anderson (1998) provide details on the observing program and the complexities of the modeling. Stone et al. (2002) described how a large number of multicolor lunar images are obtained during the two week period between the first and third quarter of the Moon, which are calibrated against frequent observations of standard stars. Stone and Kieffer (2004) estimated the averaged uncertainty in the process-

ing at 3% while the relative consistency is 1.5% in the visible and 2.5% in the near infrared (Stone et al., 2002).

Kieffer and Stone (2005) analyzed the ROLO data and derived an analytic irradiance reflectance expression:

$$\ln A_k = \sum_{i=0}^3 a_{ik} \alpha^i + \sum_{j=1}^b b_{jk} \Phi^{2j-1} + c_1 \theta + c_2 \phi + c_3 \Phi \theta + c_4 \Phi \phi + d_{1k} e^{-\alpha/p_1} + d_{2k} e^{-\alpha/p_2} + d_{3k} \cos[(\alpha - p_3)/p_4] \quad (1)$$

that expresses the disk integrated surface reflectance (the fraction of sunlight reflected by the Moon) as a function of solar phase angle ( $\alpha$ ) at the 32 ROLO wavelengths (index  $k$ ) between 0.35 and 2.45  $\mu\text{m}$ . They account for the irradiance asymmetry with respect to phase angle that they observed by allowing  $\alpha$  to be negative when the Moon is waxing and positive when waning. The selenographic latitude and longitude of the observer are  $\theta$  and  $\phi$  respectively, while  $\Phi$  is the selenographic longitude of Sun. Kieffer and Stone determined the  $a$ ,  $b$ , and  $d$  parameters for each of the 32 wavelengths and the wavelength independent  $c$  and  $p$  parameters to an estimated formal accuracy of about 1%. The irradiance model is restricted to apply between first and third quarter phases of the Moon.

\* Corresponding author.

E-mail address: [afri.rvb.pa@hanscom.af.mil](mailto:afri.rvb.pa@hanscom.af.mil) (K.E. Kraemer).



The lunar irradiance is the solar flux in a ROLO band multiplied by the reflectance at a given phase angle. The solar flux at the Moon is a function of the Sun–Moon distance while the observed lunar irradiance depends on the observer–Moon distance. For reference, Kieffer and Stone normalized their analysis to a Sun–Moon distance of 1 AU and an observer–Moon distance of 384,400 km.

The USGS effort did not attempt the ultimate goal of the absolute radiance of the full disk-resolved Moon. That is the topic of this paper. The disk-resolved lunar reflectance model presented in this paper was developed incrementally. With each step we demonstrate improvements to the model accuracy. The three stages of development are as follows:

1. We modified the scattering function of Hillier et al. (1999); (Eq. (3)) by adopting the Hapke (2002) expression for multiple scattering and coherent backscattering (Section 2.3), and adjust the parameters to match the prediction of Hillier et al. for the maria and highlands (Section 3.1). This model was subsequently compared to and refined based on the ROLO chip observations and ROLO image observations (kindly provided by T. Stone).
2. We update the model parameters for the maria and highlands by fitting to a subset of representative ROLO chip data for the “MareS” and “HighL” chips (Section 3.2.2). We found it necessary to introduce a third scattering regime in order to improve modeling for bright regions, principally craters. The parameters for the craters were trained on the ROLO “Tycho” chip (Section 3.2.2).
3. We refined the methodology of the interpolation between the models of the different surface classes and introduced basemap corrections to address an East–West bias and striping near the equator based on comparison to ROLO imagery (Section 3.3.1).

## 2. The absolute lunar radiance

To create an accurate model for the lunar radiance for an observer on the Earth’s surface or in orbit, one needs the following information:

- The geometry of the Sun, Moon, and observer including libration and nutation effects and adoption of selenographic coordinates on the reference lunar surface.
- The disk-resolved albedo or normalized reflectance.
- A scattering model for the lunar surface.
- A description of the lunar topography.
- The wavelength-dependence of the lunar reflectance.

In this paper, we combine the latest models and available observations to generate a physically accurate representation of the observed lunar radiance.

### 2.1. Geometry

We use the Jet Propulsion Laboratory lunar and planetary ephemeris DE 421 (Folkner et al., 2008; Williams et al., 2008) to position the Moon with respect to the Sun and the center of the Earth at the time of observation. DE 421 includes substantial improvements to the lunar orbit compared to the widely used DE 405 (Standish, 1998) or earlier versions, simultaneously fitting laser ranging data and planetary positional measurements through December 2007. The topocentric position of the observer and selenographic coordinates are calculated using the procedure described in Chapter 51 of Meeus (1991). From the lunar ephemeris and the selenographic coordinate system, for a particular day and time, we calculate the sub-solar point, the sub-Earth point, and the sub-observer point (which is considered a topocentric offset from the sub-Earth point). The phase angle  $\alpha$ , the angle formed

by the Sun–Moon–observer vectors, is the primary independent parameter for the reflectance model.

### 2.2. Disk-resolved reflectance

The fundamental reference for the disk-resolved lunar reflectance is the Clementine band B (0.750  $\mu\text{m}$ ) basemap. The Clementine program has made its UV–Visible data available in the form of a selection of raw images and a global basemap at 0.75  $\mu\text{m}$ . This basemap is a montage of the Clementine B filter images of the entire Moon normalized to nadir viewing ( $0^\circ$  emittance angle), a  $30^\circ$  incident angle, and a  $30^\circ$  solar phase angle. Recently, the USGS (Lee et al., 2009) released an updated basemap that addressed distortions and frame-to-frame registration errors of previous maps. The new map was derived with an improved geodetic control network and a detailed 3D shape model based on the Unified Lunar Control Network (ULCN) 2005 Digital Elevation Model (DEM). We obtained the new basemap from the Map-a-Planet web site (<http://www.mapaplanet.org>) using a nearest-neighbor extraction at 2 km resolution. The calibration of the new basemap is consistent with that of the original. Hillier et al. (1999) noted in their Appendix A that the Clementine basemap reflectance was too high with respect to previous work and derived a multiplicative correction factor of 0.532. We include this correction in our analysis. Other visible artifacts of the basemap that are addressed in our analysis include striping near zero latitude, a  $\pm$ East–West trend in reflectivity, reduced accuracy near the poles, and missing data. These corrections are discussed in Appendix B.

### 2.3. Scattering model

Hillier et al. (1999) developed both an empirical representation and a physics-based model of the disk-resolved two-terrain reflectance of the Moon based on the (renormalized) Clementine observations. A key feature of the models was that they accounted for the sharp increase in reflectance at opposition, i.e., the opposition surge, for which mechanisms were explicitly included in the physics-based model. A good representation of the opposition surge is essential for using the (nearly) full Moon for calibration.

The Hillier et al. empirical representation described the mean solar phase functions  $f(\alpha)$  for observation in the lunar maria and highlands in the five Clementine bands between 0.45 and 1  $\mu\text{m}$  indexed by  $k$  of the form

$$f_k(\alpha) = \sum_{i=0}^4 a_{ik} \alpha^i + b_{0k} e^{b_{1k} \alpha} \quad (2)$$

where the solar phase,  $\alpha$ , is positive. The fraction of collimated incident solar irradiance onto a surface element that is scattered in the direction of the observer is the reflectance and is given by

$$I/F = R(i, e, \alpha) = \frac{\mu_0}{\mu_0 + \mu} f(\alpha) \quad (3)$$

where  $I$  is the reflected flux into at the emitted angle and  $F$  is the incident solar flux for which we use a Kurucz solar model (<http://kurucz.harvard.edu/sun.html>). The Lommel–Seeliger factor,  $\mu_0/(\mu_0 + \mu)$ , is the first order representation of the scattering (limb darkening) dependence on the incident angle,  $\cos i = \mu_0$ , and the emission angle,  $\cos e = \mu$ . Table 3 of Hillier et al. lists the parameter values they derived for Eq. (2) for the maria and highlands.

For the purposes of calibration, we adopt a physics-based scattering model similar to that of Hillier et al. (1999). That model explicitly accounted for both single and multiple scattering, the shadow-hiding and coherent backscattering associated with the opposition surge, and the effect of macroscopic surface roughness.



The current model has been brought up-to-date using the expression of Hapke (2002) and is given by:

$$R(i, e, \alpha) = \frac{\varpi}{4\pi} \frac{\mu_0}{\mu_0 + \mu} [(1 + B(\alpha))P_{HG}(\alpha) + M(\mu_0, \mu)](1 + B_{0c}B_C(\alpha, h_c)) \times S(i, e, \alpha, \bar{\theta}) \quad (4)$$

where  $\varpi$  is the single scattering albedo. The singly scattered component,  $[1 + B(\alpha)]P_{HG}(\alpha)[1 + B_{0c}B_C(\alpha, h_c)]$ , is composed of three parts: a two term Henyey–Greenstein single particle scattering function:

$$P_{HG}(\alpha) = \frac{(1 - c)(1 - g_1^2)}{(1 + 2g_1 \cos \alpha + g_1^2)^{3/2}} + \frac{c(1 - g_2^2)}{(1 + 2g_1 \cos \alpha + g_2^2)^{3/2}} \quad (5)$$

a shadowing opposition enhancement term,  $1 + B(\alpha)$ , where

$$B(\alpha) = \frac{B_0}{1 + (1/h) \tan(\alpha/2)} \quad (6)$$

where  $h$  is the angular width of the shadow-hiding opposition surge and  $B_0$  is the amplitude, and finally a factor  $[1 + B_{0c}B_C(\alpha, h_c)]$  that represents the coherent backscatter term  $B_C(\alpha)$  from Hapke (2002):

$$B_C(\alpha) = \frac{1 + \frac{1}{2} \frac{e^{-1/h_c \tan(\alpha/2)}}{(1/h_c) \tan(\alpha/2)}}{2[1 + (1/h_c) \tan(\alpha/2)]^2} \quad (7)$$

According to Eq. (14) in Helfenstein et al. and Eq. (34) of Hapke (2002),  $h_c$  is physically related to the angular width,  $\Delta x_{CB}$ , of the coherent backscatter opposition surge by  $\Delta x_{CB} = 1.12 h_c$  and  $B_{0c}$  is the amplitude of the effect. Note that, unlike Hillier et al., we use the Hapke convention by having a single coherent backscatter term.

We address the parameters in the single particle scattering function following the approach of Hillier et al., who adopted the Helfenstein et al. (1997) values of  $c = 0.45$  and  $g_2 = 0.65$  describing the forward-scattering lobe of the Henyey–Greenstein function as the Clementine data could not adequately constrain these parameters and derived the value of  $g_1$  by fitting the model to the data.

As to the other scattering terms in Eq. (4), we also adopt Hapke's (2002) expression for the multiple scattering term:

$$M(\mu_0, \mu) = p(\mu_0)[H(\mu) - 1] + p(\mu)[H(\mu_0) - 1] + p^*[H(\mu) - 1] \times [H(\mu_0) - 1] \quad (8)$$

The scattered radiance into a direction,  $e$ , in the upper hemisphere by a particle when uniformly illuminated from the entire lower hemisphere is given by  $p(\mu)$ . The analogous definition for the incident angle,  $i$ , is given by  $p(\mu_0)$  while  $p^*$  is the average intensity reflected back by a particle uniformly lit from the entire lower hemisphere. Helfenstein et al. (1997) noted that the asymmetry of the Henyey–Greenstein function may be approximated by a first order Legendre function of the form  $1 - b \cos \alpha$  in which  $b = 3[(1 - c)g_1 + cg_2]$ . Adopting the first order Legendre approximation considerably reduces the computation complexity as Hapke (2002) derived an analytic solution of  $M(\mu_0, \mu)$  for the first order Legendre polynomial  $(1 + b \cos \alpha)$  in terms of the Chandrasekhar's  $H$  function and  $b$  where  $p(i) = 1 - \frac{1}{2}b \cos i$ ,  $p(e) = 1 - \frac{1}{2}b \cos e$  and  $p^* = 1 - b/4$ . Inserting these coefficients into Eq. (8) and collecting terms, we get:

$$M(\mu, \mu_0) = \left(1 - \frac{b}{4}\right)(H(\mu)H(\mu_0) - 1) - \frac{b}{2}[\mu_0 - 1/2(H(\mu) - 1) + (\mu - 1/2)H(\mu_0 - 1)] \quad (9)$$

We also adopt the more accurate approximation to  $H$  derived by Hapke (2002):

$$H(\mu) \approx \left[1 - \varpi \mu \left(r_0 + \frac{1 - 2r_0\mu}{2} \ln \frac{1 + \mu}{\mu}\right)\right]^{-1} \quad (10)$$

with  $r_0 = (1 - \gamma)/(1 + \gamma)$  and  $\gamma = \sqrt{1 - \varpi}$ , rather than the more widely used expression  $H(x) = (1 + 2x)/(1 + 2\gamma x)$ .

These expressions representing the multiple scattering and coherent backscatter terms in Eq. (4) differ from those adopted by Hillier et al. (1999). Hillier et al. assumed isotropic scattering for the multiple scattering term,  $M(\mu_0, \mu) = H(\mu_0)H(\mu) - 1$ . In this study, Eq. (9) reduces to the Hillier et al. term when  $b$  equals zero. For  $b$  not equal to zero, the contribution from multiple scattering is increased which requires a corresponding decrease in the single scattering albedo to match the observations. In addition, the more recent expression for the coherent backscatter function from Hapke (2002) is adopted. The Hapke approximation was based on an analytic expression derived for the random walk of photons in a scattering medium. The characteristic width of the coherent backscatter derived from the model is related to the mean transport free path, a relationship that Hapke notes has experimental validation. Also, Hapke's expression is analytic, which is much more computationally concise than the interpolative procedure used by Hillier et al. Its behavior as a function of phase is presented in Fig. 2 where it is shown to be functionally distinct from that adopted by Hillier et al.

Finally, we include the Hapke (1984) surface roughness function,  $S(i, e, \alpha, \bar{\theta})$ . This expression accounts for shadowing due to the macroscopic roughness of the surface and is defined by the average slope tilt,  $\bar{\theta}$ . Hapke (1984) assumed that the reflectance of the rough surface can be related to the smooth surface by multiplying by a shadowing factor,  $S$ , which accounts for a decrease in the overall intensity of the light and, more importantly, that the incident and emission angles are modified because of the slope of the facets. The relationship between smooth and rough surface reflectance is:

$$R_R(i, e, \alpha) = R_S(i', e', \alpha)S(i, e, \alpha) \quad (11)$$

where  $i'$  is the incident angle for a tilted facet;  $e'$  the emission angle from a tilted facet;  $\mu' = \cos e'$  and  $\mu'_0 = \cos i'$  which are depicted in Fig. 1.

Hapke (1984) solves for surface roughness shadowing for cases with  $i \leq e$  and  $i > e$  as follows:

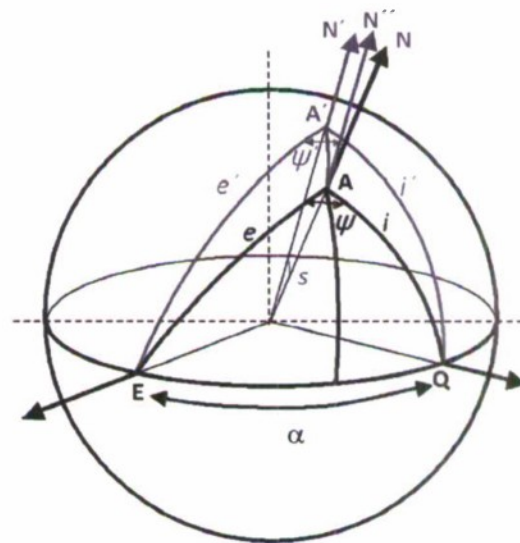


**Fig. 1.** The geometry and notation used in the photometric model is illustrated. The observer is at a position such that the sub-observer location is  $E$  and the Sun has sub-solar position  $Q$ . The phase angle,  $\alpha$ , is angle between the observer and Sun positions. The normal  $N$  at location  $A$  is the normal for an assumed spherical Moon and the normal  $N'$  at location  $A'$  is the effective normal for a sloped surface. The slope angle  $s$  is the angle between  $N$  and  $N'$ . The incidence and emission angles measured relative to the spherical surface and the sloped surface are  $(i, e)$  and  $(i', e')$  respectively. The azimuthal angles  $\psi$  and  $\psi'$  are the angles between the projection of the incidence and emission angles onto the surface.



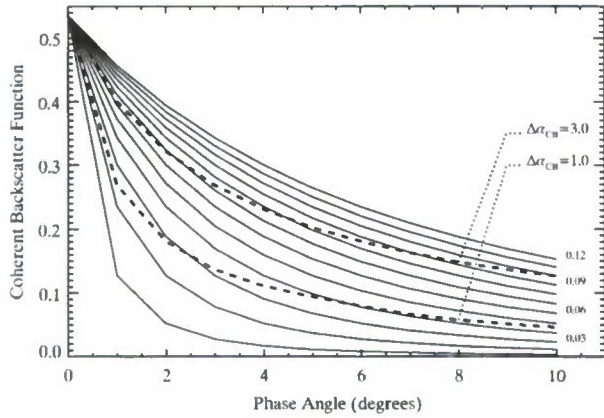


**Fig. 2.** Comparison of the Hapke Coherent backscatter function for  $h_c = 0.01\text{--}0.12$  (solid lines) with the model (dashed lines) used by Hillier et al. for widths  $\Delta\alpha_{CB} = 1.0$  and  $3.0^\circ$  (i.e., within the range determined by Hillier et al. for the highlands in Clementine band B). The curves are scaled to match the Hillier et al. model at phase angle  $\alpha = 0^\circ$ . The ratio of the Hillier et al. derived values and  $h_c$  is roughly  $40^\circ$ .

$$S = \begin{cases} \frac{\mu'_0}{\mu_0} \frac{\mu_0}{\mu'_0} \frac{1}{\sqrt{1+\tan^2 \bar{\theta}}} \left[ 1 - f + \frac{f}{\sqrt{1+\tan^2 \bar{\theta}}} \frac{\mu_0}{\mu'_0} \right]^{-1} & i \leq e \\ \frac{\mu'_0}{\mu_0} \frac{\mu_0}{\mu'_0} \frac{1}{\sqrt{1+\tan^2 \bar{\theta}}} \left[ 1 - f + \frac{f}{\sqrt{1+\tan^2 \bar{\theta}}} \frac{\mu}{\mu'_0} \right]^{-1} & i > e \end{cases} \quad (12)$$

where

$$f(\Psi) = e^{-2 \tan(\frac{\Psi}{2})} \quad (13)$$

and the azimuthal angle  $\Psi$  is given by:

$$\cos \Psi = \frac{\cos \alpha - \cos i \cos e}{\sin i \sin e} \quad (14)$$

with the range  $0 \leq \Psi \leq \pi$ . The quantity  $f(\Psi)$  is defined based on the illumination shadow (i.e., areas not visible due to shadowing) and the visibility shadow (i.e., areas not visible due to the tilt angle of the surface facet). For  $i \leq e$ ,  $f(\Psi)$  is the fraction of the illumination shadow hidden in the visibility shadow and for  $i > e$ ,  $f(\Psi)$  is the fraction of the visibility shadow hidden in the illumination shadow. These equations are equivalent to Eqs. (52), (32), and (3) in Hapke (1984) (although the first part of Eq. (12) is not numbered but appears between his Eqs. (49) and (50)). The formulations for the various  $\mu$ 's are also adopted from Hapke (1984) but not reproduced here. We assume the values of  $\bar{\theta} = 27^\circ$  for highlands (and craters) and  $\bar{\theta} = 24^\circ$  for maria in the shadowing expression, as suggested by Helfenstein and Shepard (1999) and adopted by Hillier et al. (1999). Hillier et al. also demonstrated that their model at the Apollo 16 site was consistent with this slope tilt. These slope angles are consistent with the values of  $22.2^\circ \pm 1.3^\circ$  (maria) and of  $34.1^\circ \pm 2.6^\circ$  (highlands) recently derived by Goguen et al. (2010), who assumed a rough single-scattering surface. Our values are also in agreement with the  $33^\circ$  value from the Hartman and Domingue (1998) analysis of the lunar irradiance phase.

#### 2.4. Topography

We adopted the 2 km surface element Clementine basemap as our working database. Thus, the sub-Earth element has a  $\sim 1^\circ$  angular extent viewed from the Earth or near Earth orbit. This is sufficient for calibration for most sensors. We include the lunar surface geometry using the topographic map obtained from laser altimetry measurements by the Japanese Aerospace Exploration Agency (JAXA) sponsored Kaguya lunar orbiter mission. The

Kaguya altimetry data represents substantial vertical and spatial resolution advantages over the first lunar topographic map providing uniform global coverage, the Unified Lunar Control Network (ULCN 2005) model. The Kaguya altimetry provides 5 m vertical resolution (Sasaki et al., 2008) and generated  $6.77 \times 10^6$  geolocated data points over the full lunar surface (Araki et al., 2009), compared to 272,931 points included in the ULCN 2005 dataset (Archinal et al., 2006). The Kaguya team interpolated the altimetry data to a  $1/16^\circ$  grid resulting in a topographic map size of  $5760 \times 2880$  elements. This translates into an element size of 1.9 km, a good match to the 2 km basemap.

The topography introduces a change in the local vertical direction for a given element in the baseline map, which is used in the photometric model. The geometry associated with topographic tilt is similar to the specification of macroscopic surface roughness slope presented in Fig. 1. The normal,  $N$ , is tipped by an angle,  $s$ , from the reference sphere normal,  $N$  as derived from the topographic model. The azimuthal angle between the incident angle,  $i$  and  $s$  is  $\zeta$  while that between  $e$  and  $s$  is  $v$ . The modified direction cosines are then:

$$\mu'_0 = \cos i' = \cos i \cos s + \sin i \sin s \cos \zeta \quad (15)$$

and

$$\mu' = \cos e' = \cos e \cos s + \sin e \sin s \cos(\zeta - v) \quad (16)$$

In practice, the modified direction cosines are determined by computing the surface normal at a given location and evaluating the angle between the normal and the vector pointed at the observer and the Sun. Our model computes the surface normals based on the Kaguya topography. The 2-km scale of the topography is considerably larger than that of the surface roughness that is represented by the mean tilt angle in the shadowing expression. In our implementation, the modified direction cosines due to topography are evaluated to determine the effective incident and emission angles at the surface. These in turn are used to compute the angle-dependent correction for sub-resolution surface roughness described in Eq. (12).

#### 2.5. Terrain regimes and the albedo

Various theoretical considerations indicate that the surface albedo is the first order dependent variable that modifies the scattering function; that is, different scattering function parameters are needed for different albedos. For the Moon, terrain is a reasonably good indicator of albedo; hence the Hillier et al. analysis of maria and highlands. Neither the maria nor highland classification is perfect however, as bright lunar crater ejecta occur in the maria, and surface roughness also plays a role (e.g. Appendix C of Hillier et al.).

The distribution of basemap reflectance (as a surrogate for albedo) as a function of terrain height is shown in Fig. 3. The distribution clearly separates into two concentrations of albedo at different altitudes, the maria and the highlands. The plot shows that the reflectances cluster around values of 0.05 and 0.1 with a broad range of more sparsely populated values. A high surface reflectance "tail" associated with bright craters and ejecta is also evident in the figure. Appendix A of Hillier et al. (1999) describes the process they used to calibrate the Clementine band B data based on the observations of Shorthill et al. (1969), and the data in Fig. 3 have been corrected by the factor of 0.532 mentioned in Section 2.2. The 15 calibration regions used to determine the correction factor that Hillier et al. identified as "dark", "average", and "bright" regions are noted in the figure.

A general model of reflectance,  $R(i, e, \alpha)$ , that can account for multiple surface types at any given location and wavelength is computed as the linear combination of the modeled reflectance



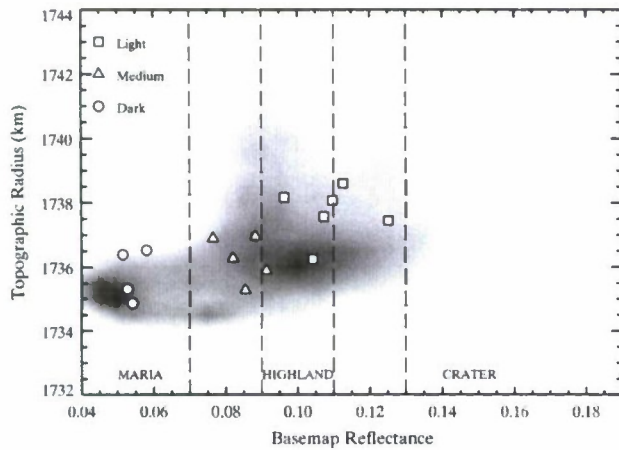


Fig. 3. Basemap reflectance plotted against height. A distinct separation between the concentrations for the highlands and maria is evident although there is a continuum of points at lesser density between the two. Regions that Hillier et al. labeled as having “dark”, “medium”, and “light” albedo are denoted with circles, triangles, and squares, respectively.

$R_{MOO,k}(i, e, \alpha)$  (represented by Eq. (4)) for each surface type  $k$ , scaled by the ratio of the basemap reflectance  $R_{BM}$  to the reference reflectance  $R_{REF,k}$ , and multiplied by the weighting factor  $c_k$ .

$$R(i, e, \alpha) = \sum_{k=1}^N c_k \left( \frac{R_{BM}}{R_{REF,k}} \right) R_{MOO,k}(i, e, \alpha) \quad (17)$$

The values of  $R_{REF,k}$  are determined by the locations/conditions for which the model is derived. The weighting factors  $c_k$  vary between 0 and 1 and are a function of the basemap reflectance and surface classification. The next section specifies the reference reflectance term and how the surface types were determined that contribute to the model reflectance at a given location.

## 2.6. Spectral representation

The scattering model was trained with observations in a particular set of bandpasses. For example, Hillier et al. (1999) derived model coefficients for the 0.415, 0.750, 0.900, 0.950, and 1.0  $\mu\text{m}$  Clementine bands A–E, respectively. To compute the reflectance at any wavelength, our model band reflectances are spectrally interpolated following the procedure suggested by Kieffer and Stone (2005), in which a lunar reflectance spectrum from the Apollo 16 soil sample is fit to the model band-predicted reflectances by applying an  $a + b\lambda$  scaling factor. The lunar spectrum spans the wavelength range of 0.35–2.45  $\mu\text{m}$ , and was measured in the laboratory using a soil sample collected at the Apollo 16 landing site.<sup>1</sup> As an example, the fits to reflectance for highlands and maria, obtained with the ROLO instrument, are shown in Fig. 4. Note that since the thermal emission from the lunar surface contributes as much as ~10% to observations in the longest-wavelength bands, the two long wavelength bands are not used in computing the fitted spectrum. The effect of thermal emission on the ROLO long wavelength band measurements and an assessment of errors incurred when using thermal-sensitive bands to fit the lunar spectrum is included in Section 3.2.2. The reflectance in any band can be computed from the scaled spectral reflectance by integrating over the spectrum weighted by the instrument spectral response function. To get the amount of reflected radiance from the Moon, Eq. (4) is multiplied by the in-band solar flux at the instantaneous Sun–Moon distance, which is the integral over wavelength of the spectral energy

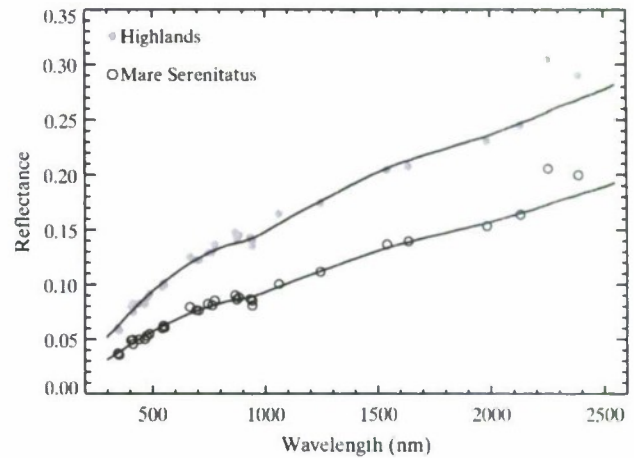


Fig. 4. Spectral reflectance of the Moon in the visible and infrared ROLO bands. The plot shows the highland and maria reflectance for the 23 ROLO VIS–NIR bands and the nine SWIR bands. The appropriately scaled Apollo 16 soil spectrum is superimposed for each terrain type. The ROLO bands at 2.256 and 2.390  $\mu\text{m}$  (Bands 66 and 68, respectively) are indicated on this plot but are not used in scaling the reflectance spectrum as these bands contain a non-negligible thermal contribution.

distribution of the Kurucz solar irradiance model times the instrument spectral response.

## 3. Model development and performance analysis

### 3.1. The updated reflectance model

In their formulation of the problem, Hillier et al. (1999) computed reflectance models for two surface classes: maria and highlands. With the more accurate representation developed in this paper, it was necessary to re-derive values of the free parameters in Eq. (4), viz., the albedo,  $\varpi$ , the asymmetry parameter in the Henyey–Greenstein function,  $g_1$ , the shadow-hiding and coherent-backscatter amplitudes,  $B_0$  and  $B_{0c}$ , respectively, and their characteristic widths,  $h$  and  $h_c$ . Previous studies, as well as the current work (see below), have demonstrated that bidirectional reflectance measurements do not contain sufficient information to constrain all of the free parameters. Therefore, in order to reduce the dimensionality of the problem, we adopt values from the literature for the terms describing the forward scattering lobe of the Henyey–Greenstein function. As previously noted, Hillier et al. fixed the value of  $g_2$  at 0.65 and the fractional contribution of the forward scattering term (involving  $g_2$ )  $c$  at 0.45, values we also adopt. Since  $g_2$  and  $c$  are fixed, calculating  $g_1$  determines  $b$  in the multiple scattering term. We applied a  $\chi^2$  fit to the Hillier et al. model predictions for the maria and highland regions for the geometry  $e = 0^\circ$  and  $i = \alpha = 30^\circ$  in the five Clementine wavebands to update our model under the above assumption and specifically including multiple scattering.

The results of fitting the model made clear that the scattering problem does not have a unique solution, as has been previously noted by many others (e.g. Hapke, 2002; Shepard and Helfenstein, 2007). Among a continuum of possible solutions for the opposition surge terms, a narrow coherent backscatter and wide shadow-hiding function may be derived or with the reverse. A solution was found for the values of  $\varpi$ ,  $g_1$ ,  $B_0$ ,  $B_{0c}$ ,  $h$  and  $h_c$  that minimized  $\chi^2$  difference with the Hillier et al. model, for each waveband and surface class. For each element of the four-dimensional space defined by the amplitude and width terms  $B_0$ ,  $B_{0c}$ ,  $h$  and  $h_c$ , we found the best solution for  $\varpi$  and  $g_1$  for each Clementine waveband via a downhill simplex minimization scheme. A sample of the results is shown

<sup>1</sup> <http://planetary.brown.edu/pds/AP62231.html>

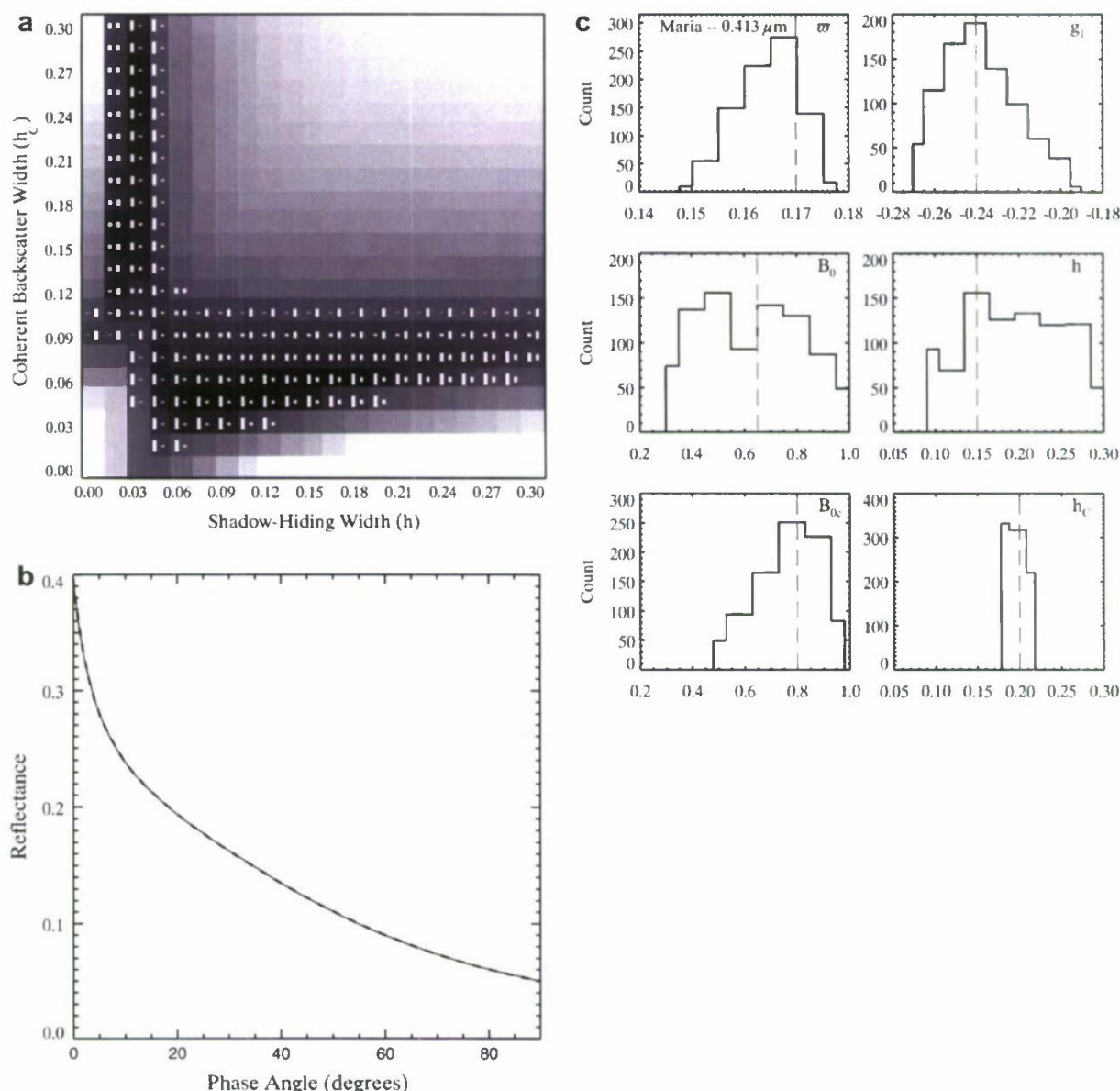


**Fig. 5.** The reflectance model for the highlands in Clementine band B is derived using a down-hill simplex minimization as a function of the shadow-hiding and coherent-backscatter widths (left). The solution is represented as the chi-square difference relative to the Hillier et al. model. The best-fit solutions are represented by the dark squares. The vertical bars indicate the amplitudes of the shadow-hiding (left bars) and coherent backscatter (right bars) terms. For this case, a solution is adopted with  $h = 0.15$  and  $h_c = 0.06$ . On the right, this solution (dashed line) is compared to the Hillier et al. model (solid line). The opposition surge is represented by the sharp increase in reflectance for small phase angles. The models agree to well within 1%. Example of the frequency distributions of the possible solutions for the fitted parameters. The dashed vertical lines indicate the selected values.

in Fig. 5, which displays the  $\chi^2$  fit as a function of the shadow-hiding and coherent-backscatter widths for the highlands. The value of  $\chi^2$ , the magnitude of which is represented by the gray scale with the darkest shades representing the best fit (lowest  $\chi^2$ ), is the minimum value over the range of amplitudes for the shadow-hiding and coherent-backscatter effects. The relative amplitudes of these contributors are represented as vertical bars for solutions with the lowest  $\chi^2$  values.

To determine the best-fit model with uncertainties, we evaluated the frequency distribution of each parameter for those solutions with  $\chi^2$  below a specified threshold (Fig. 5c). Typically,  $\chi^2 < 0.7$  was used but this threshold was relaxed if an insufficient number of solutions qualified. The model parameters are selected by indentifying the multi-dimensional subset of parameter space

which, in combination, fit the observations. The selected values are shown by the vertical dashed lines in the figure; note that they do not necessarily correspond to the peaks in the distributions because the parameters were determined as a set, not individually. Following Hillier et al. (1999) and Hapke (2002), solutions were restricted to exclude those with a wide coherent backscatter surge and a narrow shadow-hiding surge. The analysis indicated that model parameters  $g_1$ ,  $w$ , and  $h_c$  are well-constrained, but that  $h$  and the amplitude terms  $B_0$  and  $B_{0c}$  are weakly constrained.

Because shadow-hiding is a geometrical effect that depends on surface particle size distribution,  $\Delta\alpha_{SH} = 2h$  should be independent of wavelength. Values of  $h$  were empirically estimated for both the highlands and maria, and adopted in all wavebands, which was ultimately fixed at 0.15 (approximately  $17^\circ$ ). Although, this value



**Table 1**

Parameter solutions at Clementine wavebands for maria from the updated reflectance model.

Band ( $\mu\text{m}$ )	$\varpi$	$g_1$	$B_0$	$h$	$B_{0c}$	$h_c$
A: 0.415	0.193	−0.281	1.00	0.15	0.75	0.075
B: 0.750	0.326	−0.211	1.00	0.15	0.60	0.120
C: 0.900	0.334	−0.218	0.95	0.15	0.65	0.105
D: 0.950	0.331	−0.216	1.00	0.15	0.60	0.120
E: 1.00	0.320	−0.241	1.00	0.15	0.45	0.105

**Table 2**

Parameter solutions at Clementine wavebands for highlands from the updated reflectance model.

Band ( $\mu\text{m}$ )	$\varpi$	$g_1$	$B_0$	$h$	$B_{0c}$	$h_c$
A: 0.415	0.328	−0.307	0.95	0.15	0.45	0.075
B: 0.750	0.480	−0.324	0.80	0.15	0.35	0.060
C: 0.900	0.518	−0.309	0.80	0.15	0.30	0.060
D: 0.950	0.525	−0.289	0.95	0.15	0.25	0.060
E: 1.00	0.549	−0.307	0.50	0.15	0.45	0.030

agrees quite well with the 0.158 value derived by Helfenstein et al. (1997) for their best model (Solution 2a) in their analysis of the lunar opposition surge, it is two to three times larger than Hillier et al.'s values. As may be seen in Fig. 2, the wings of the Hapke coherent backscatter function adopted in the present model decline more steeply with phase angle than it does in the formalism of Orzin (1992) that is used by Hillier et al. This will tend to increase the shadow-hiding width  $h$  to compensate, but not by a factor of two. In fact,  $h$  is not well-constrained by the model, and a wide distribution of values produced satisfactory fits. We selected the value of  $h = 0.15$  as it is suitable for the full range of wavebands and surface types.

The derived parameters for the maria and highlands are tabulated in Table 1 and 2, respectively, which may be compared to the Hillier et al. (1999) model parameters in their Tables Vb and Va, respectively. To facilitate the comparison, the coherent backscatter angle is  $\sim 40^\circ \times h_c$ . The agreement is reasonable given the uncertainties cited by Hillier et al. The values derived herein for the single scattering albedo and the asymmetry parameter are consistent with those of Hillier et al. to about 3% and 7% respectively. However, the widths and amplitudes of the shadow-hiding and coherent backscatter terms differ. For this model, we did not compute formal estimates of the errors in our derivation since the comparison was with the Hillier model and not data. However, we estimate that a  $\pm 0.05$  error in the shadow-hiding width corresponds to an uncertainty of about 2% in the single scattering albedo.

The general model for the surface reflectance as a function of surface albedo and terrain type (Eq. (17)) was introduced in Section 2.5. Initially, we proposed a two-component model consisting of maria and highlands, which were separated by an intermediate region of mixed type. In that case, we defined the models M (maria) and H (highlands) as follows:

Maria	$R_{BM} \leq 0.07$	$C_M = 1$	$C_H = 0$
Intermediate	$0.07 < R_{BM} < 0.09$	$C_M = (R_{BM} - 0.09)/0.02$	$C_H = (R_{BM} - 0.07)/0.02$
Highlands	$R_{BM} \geq 0.09$	$C_M = 0$	$C_H = 1$

where  $R_{BM}$  is the Clementine basemap reflectance at a given location. In this formulation, the quantities  $R_{REF,M}$  and  $R_{REF,H}$  (in Eq. (17)) represent the values of basemap reflectance (i.e., at  $i = 30^\circ$ ,

$e = 0^\circ$ ,  $\alpha = 30^\circ$ ) [i.e.,  $R_{REF,M} = R_{MOD,M}(30^\circ, 0^\circ, 30^\circ) = 0.0655$  and  $R_{REF,H} = R_{MOD,H}(30^\circ, 0^\circ, 30^\circ) = 0.1207$ ]. In their application of the model to the Clementine data, Hillier et al. (1999) combined observations from many locations that they identified either as maria or highlands. To address the variation in albedo within these classes, a normalization factor was applied to each image region based on the difference from the mean for all regions within a class. This implies that the values of  $R_{REF,M}$  and  $R_{REF,H}$  represent average conditions. This model assumes that the surface reflectance can be distinctly modeled as either maria (for dark regions) or highlands (for bright regions) with intermediate regions taken as a mix of these two categories.

### 3.2. Model development and analysis based on the ROLO chip dataset

When compared to the independent ROLO dataset, the two-component maria and highlands model based on Hillier et al. was found to be inadequate in the sense that to the bright cratered regions were discrepant. Furthermore, the ROLO data afforded the opportunity to extend the reflectance model through shortwave infrared bands to approximately  $2 \mu\text{m}$ . This section describes the analysis and refinement of the lunar calibration model based on ROLO chip data (i.e., calibrated radiances for selected sites adopted by the ROLO program; see Kieffer and Stone, 2005). We begin with an assessment of the accuracy of the updated reflectance model, and then introduce refinements to the model by fitting to the ROLO chip data directly. The performance of the model is expressed in terms of the accuracy (i.e., the average bias between the model and the data) and the precision (i.e., the standard deviation of the residuals with respect to the mean bias). Both quantities are expressed as a percentage relative to the observed value.

#### 3.2.1. Assessment of the updated model

To assess the accuracy of the modeled reflectance fitted to the Hillier et al. model, we compared the model predictions to ROLO data for the 11 sites, shown in Fig. 6, which Kieffer and Stone (2005) used to derive the lunar irradiance. The ROLO processing creates a modified Lambert azimuthal equal-area projection (that Kieffer and Stone label as the "ALEX" projection) normalized in solar and geocentric distances and large enough to project the 59% of the lunar surface that is visible from the Earth over time due to nutation and libration. The locations of the ROLO chips are specified by selenographic latitude and longitude and as a range of indices in the ALEX projection, all of which are given in Table 3 of Kieffer and Stone (2005). The ROLO data include the observed radiances for  $3 \times 3$  (or  $7 \times 7$ ) groups of ROLO pixels at each site and phase angle and the sub-observer and sub-solar selenographic coordinates for the time of observation. The ROLO chip observations as a function of phase angle are reproduced in Fig. 7. The asymmetry in the reflectance curve versus phase angle at a given location is largely governed by asymmetries in the incidence angle and is particularly pronounced for positions near the edge of the Moon. The scatter in these observations is due to differences in the incidence and emergence angles resulting from the lunar

libration. The lunar opposition effect (to which both shadow-hiding and coherent backscatter contribute) is evidenced by the abrupt increase in reflectance near zero phase angle.



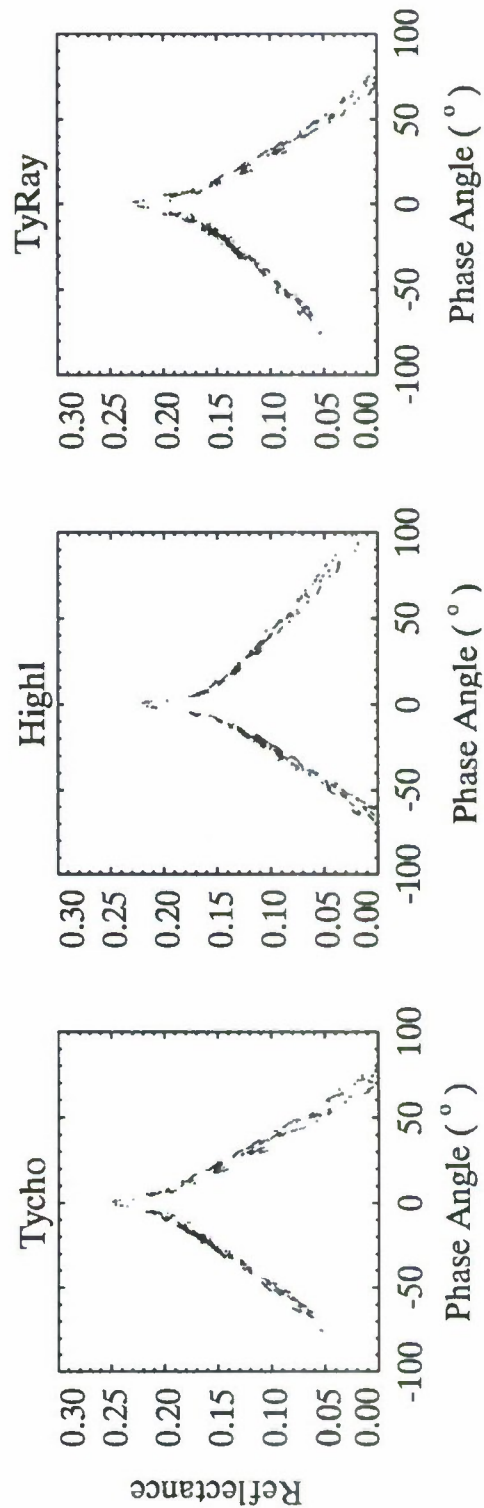
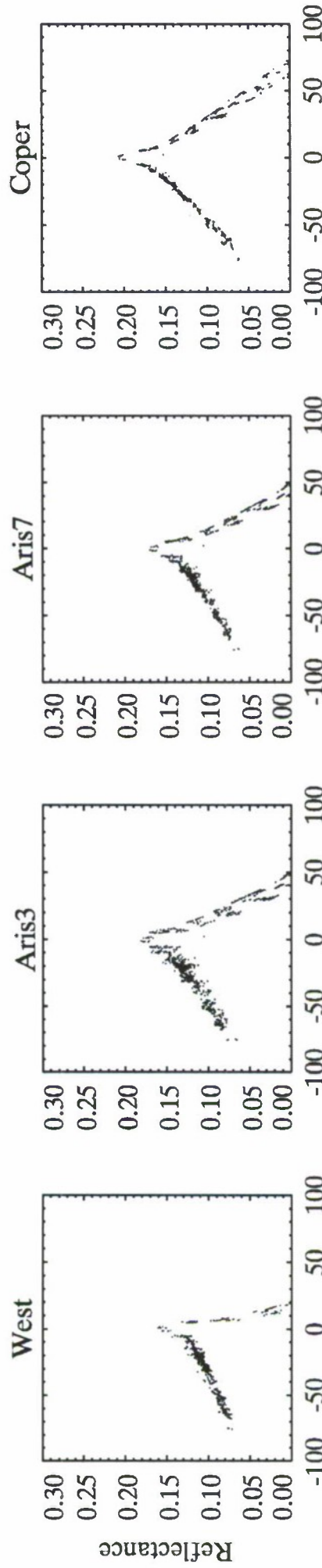
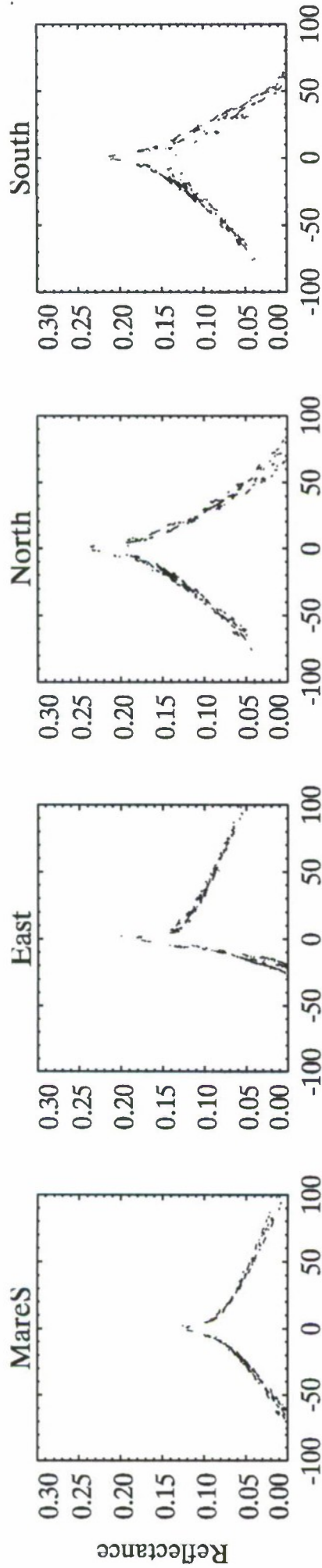


Figure 7

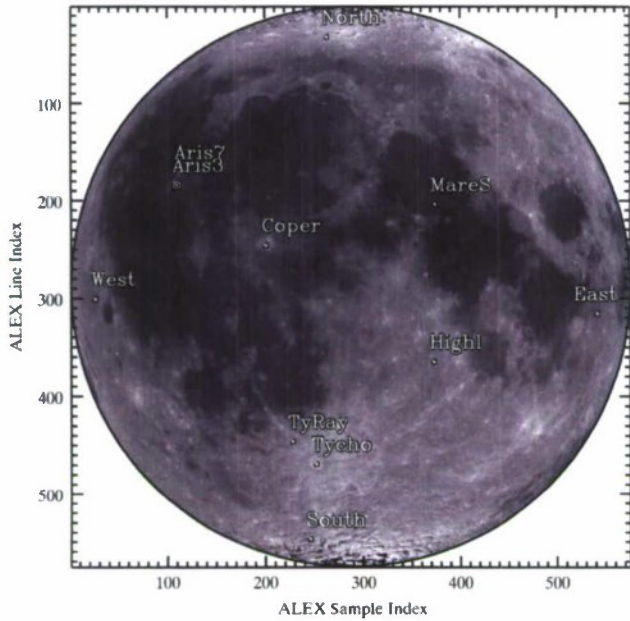


Fig. 6. The locations of the 11 ROLO sites for which reflectivities were extracted by Kieffer and Stone (2005). The sites are shown on the basemap in the normalized ALEX projection of the Moon used by the ROLO program. The ROLO "chips" are comprised of  $3 \times 3$  (or  $7 \times 7$  for "Aris7") blocks of pixels in the ALEX projection.

The sub-observer and sub-solar selenographic coordinates of the ROLO chips are computed by the reflectance model for the observation time using the lunar ephemeris. The phase angle and the incident and emergent angles are calculated from this information, taking the surface topography into account. The model reflectances were computed for the Clementine bands from the updated

two-terrain reflectance model for the ROLO geometry. The reflectances in the ROLO bands were calculated by integrating the spectrally-interpolated reflectance, derived from the direct model calculations, over the ROLO bands, assuming a square spectral response function. The performance of this model was evaluated in five ROLO bands (at 0.413, 0.550, 0.667, 0.747, and 0.868  $\mu\text{m}$ ).

Fig. 8 shows the residuals (reflectance model minus ROLO Band 12 observations) as a function of phase angle; the 0.747  $\mu\text{m}$  wavelength of ROLO band 12 is nearest to that of the Clementine base-map. In this analysis, the chip regions identified as "MareS" and "Highl" are modeled as maria and highlands respectively, while the other ROLO chips are modeled using Eq. (17). Note that the "N", "S", "E", and "W" chips are located close to the limb and have emittance angles greater than the  $70^\circ$  limit that we have imposed for the best fit for calibration. Other regions are located within large craters or ejecta ("Aris3", "Aris7", "Coper", "Tycho", "TyRay") for which the model performance is degraded. In particular, the "Aris3" and "Aris7" chips are associated with the large bright Aristarchus crater, which is viewed at high emittance angle. These performance results, represented as a model bias and RMS error, are summarized in Table 3 under the heading "VIS-NIR Clementine", with detailed results given in Appendix A. For both maria and highlands, the model bias is approximately 6%. Although the model performance is encouraging, better results may be obtained by fitting to the ROLO observations directly, which is the next step in the model development.

### 3.2.2. Model refinements using ROLO chip observations

We improved upon the scattering parameters by fitting the model directly to the ROLO chip observations. Initially, the parameters were derived based on fits to the ROLO "MareS" and "Highl" chip datasets in a similar fashion to that used to fit the Hillier et al. model predictions. Because the solution is not unique, a single model was selected after exploring the parameter space.

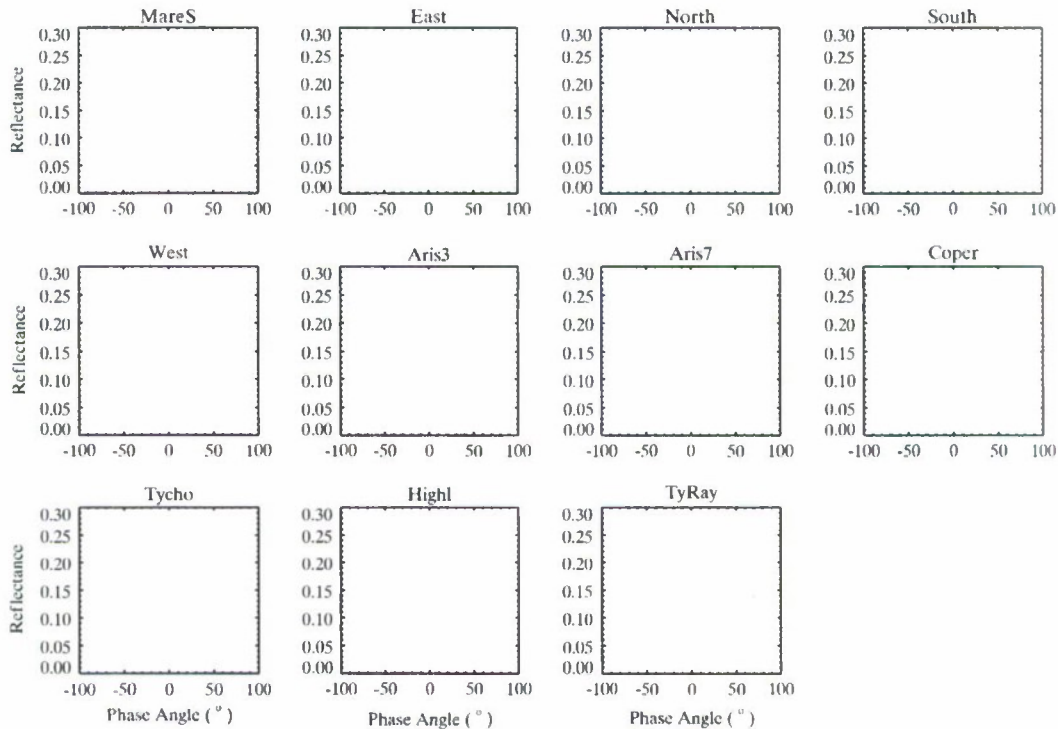
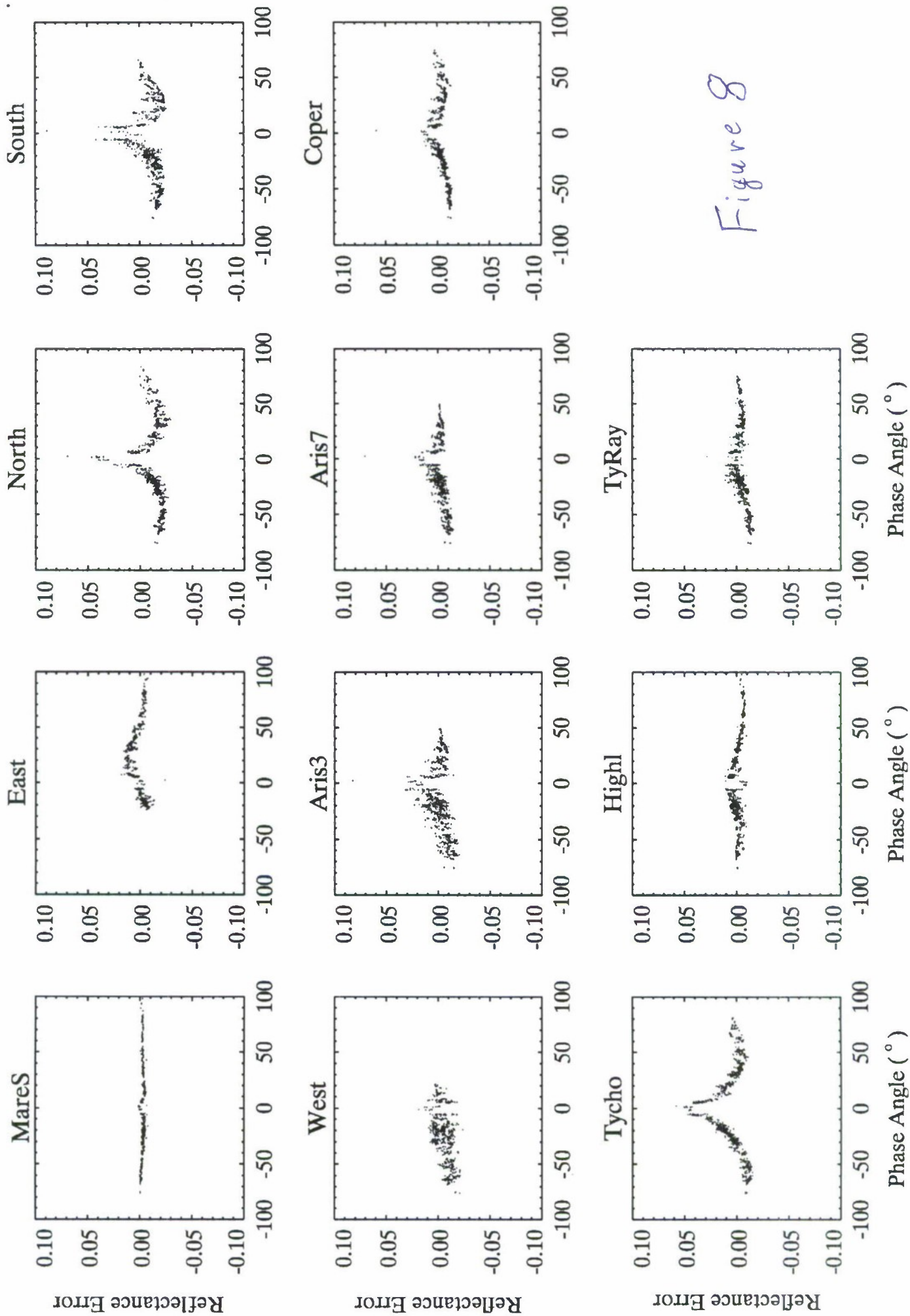


Fig. 7. ROLO reflectance at 0.747  $\mu\text{m}$  as a function of phase angle for the 11 chip locations. The asymmetry is a function of asymmetries in the incidence angles as a function of position. Near zero phase angles, the opposition surge is illustrated by the sharp increase in reflectance.





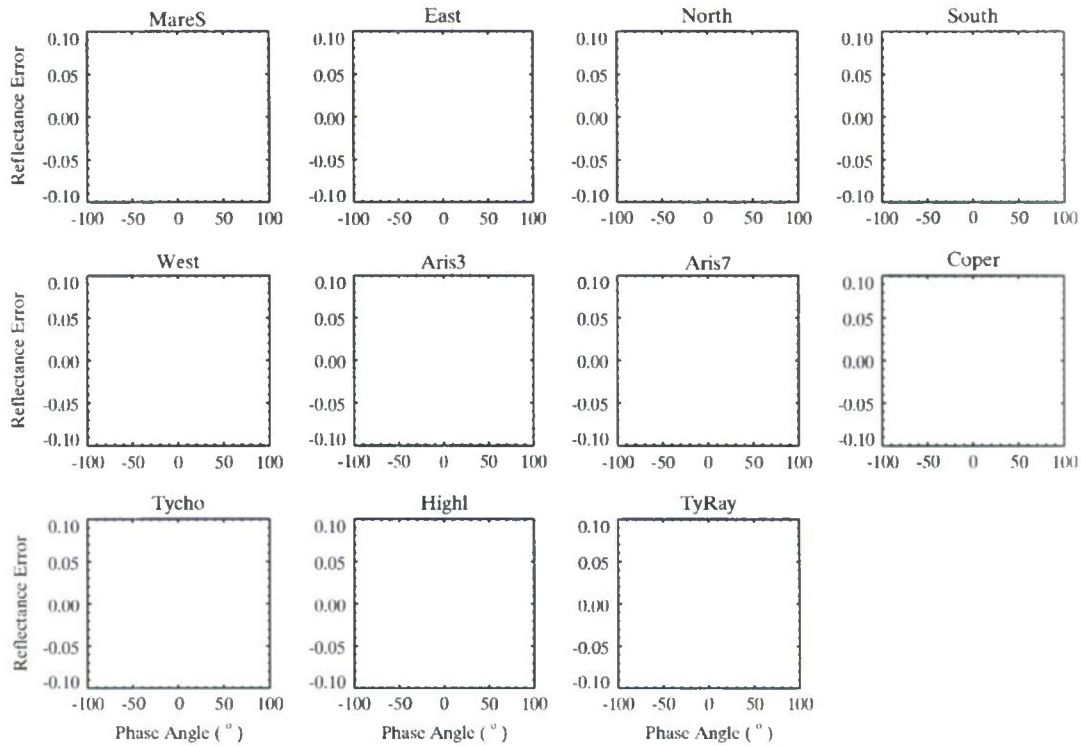


Fig. 8. Reflectance residuals versus phase angle for the ROLO chip locations. The ROLO 0.747  $\mu\text{m}$  observations are compared to the two-component Clementine reflectance model with parameters derived from the model results of Hillier et al. (1999).

Table 3

Performance summary based on ROLO chip observations.

Chip	VIS-NIR Clementine		VIS-NIR ROLO (2 component)		VIS-NIR ROLO (3 component)		SWIR ROLO (3 component)				
	Bias	RMS	Bias <sup>a</sup>	RMS	Bias <sup>a</sup>	RMS	Bias <sup>a</sup>	RMS			
1. Mare5	6.2	2.1	3.2	(2.7)	1.4	2.5	(1.9)	1.7	3.3	(4.1)	2.8
6. Aris3	11.3	14.3	15.9	(15.8)	5.4	8.4	(10.4)	7.2	11.6	(10.7)	5.0
7. Aris7	8.4	8.5	12.9	(12.9)	3.7	6.4	(8.4)	4.8	11.4	(10.6)	3.8
8. Coper	3.7	5.2	7.6	(7.6)	3.1	1.9	(3.2)	3.9	2.1	(2.4)	3.3
9. Tycho	6.1	14.8	26.2	(26.2)	3.7	1.6	(2.6)	5.3	3.6	(2.7)	5.5
10. Highl	5.9	3.8	3.5	(2.6)	2.3	3.6	(2.6)	2.9	2.1	(3.0)	2.6
11. TyRay	6.6	4.7	10.4	(13.7)	2.1	4.7	(5.4)	2.6	6.2	(6.8)	2.8

<sup>a</sup> The first bias sub-column compares the model with parameters derived in each band from the ROLO chip data with the ROLO chip observations. The second sub-column is a similar comparison but with model albedos derived by scaling the Apollo 16 soil sample spectrum to the model derived albedos in the individual bands. It is a (spectral) estimate of the bias likely in a user-defined band.

To compute the reflectance for a given chip, the lunar reflectance image is simulated at the spatial resolution and sampling of the ROLO instrument, then mapped into the ALEX projection, and finally averaged over the pixels within the chip location. However, due to the computational burden associated with the search over parameter space, it was not practical to implement the training in this way. Instead the training was performed by matching model predictions to the ROLO observations based on an averaged albedo and topographic slope at the chip location. This approximation is

expected to introduce only small errors in the optimization of the model parameters (as suggested by the results of the performance analysis). Also, the training was exercised for a random subset of the 1074 observations from the chip dataset. The model was developed initially for the 5 ROLO bands covering a similar spectral range as Clementine, specifically, ROLO Band 4 at 0.413  $\mu\text{m}$ , Band 8 at 0.550  $\mu\text{m}$ , Band 10 at 0.667  $\mu\text{m}$ , Band 12 at 0.747  $\mu\text{m}$ , and Band 14 at 0.868  $\mu\text{m}$ . The model parameters for maria and highlands are summarized in Table 4 and 5.

Table 4

Parameter solutions for the maria regime for VIS-NIR bands based on ROLO chip observations.

Band	$\omega$	$g_1$	$B_0$	$h$	$B_{0c}$	$h_c$
ROLO02 (0.413 $\mu\text{m}$ )	$0.17 \pm 0.01$	$-0.24 \pm 0.04$	$0.65 \pm 0.3$	0.15	$0.8 \pm 0.2$	$0.2 \pm 0.02$
ROLO08 (0.550 $\mu\text{m}$ )	$0.21 \pm 0.01$	$-0.24 \pm 0.04$	$0.7 \pm 0.3$	0.15	$0.75 \pm 0.2$	$0.13 \pm 0.02$
ROLO10 (0.667 $\mu\text{m}$ )	$0.26 \pm 0.01$	$-0.28 \pm 0.04$	$0.8 \pm 0.3$	0.15	$0.6 \pm 0.2$	$0.08 \pm 0.01$
ROLO12 (0.747 $\mu\text{m}$ )	$0.27 \pm 0.02$	$-0.25 \pm 0.03$	$0.8 \pm 0.3$	0.15	$0.6 \pm 0.2$	$0.08 \pm 0.01$
ROLO27 (0.777 $\mu\text{m}$ )	$0.29 \pm 0.01$	$-0.24 \pm 0.04$	$0.8 \pm 0.3$	0.15	$0.6 \pm 0.2$	$0.12 \pm 0.01$
ROLO14 (0.869 $\mu\text{m}$ )	$0.30 \pm 0.02$	$-0.27 \pm 0.03$	$0.75 \pm 0.3$	0.15	$0.6 \pm 0.2$	$0.11 \pm 0.01$



**Table 5**

Parameter Solutions for the highlands regime for VIS–NIR bands based on ROLO chip observations.

Band	$\varpi$	$g_1$	$B_0$	$h$	$B_{0c}$	$h_c$
ROLO02 (0.413 $\mu\text{m}$ )	$0.30 \pm 0.02$	$-0.31 \pm 0.05$	$0.7 \pm 0.3$	0.15	$0.6 \pm 0.2$	$0.06 \pm 0.01$
ROLO08 (0.550 $\mu\text{m}$ )	$0.37 \pm 0.02$	$-0.28 \pm 0.04$	$0.7 \pm 0.3$	0.15	$0.6 \pm 0.2$	$0.09 \pm 0.02$
ROLO10 (0.667 $\mu\text{m}$ )	$0.45 \pm 0.02$	$-0.33 \pm 0.04$	$0.45 \pm 0.3$	0.15	$0.65 \pm 0.2$	$0.03 \pm 0.02$
ROLO12 (0.747 $\mu\text{m}$ )	$0.46 \pm 0.02$	$-0.32 \pm 0.04$	$0.5 \pm 0.3$	0.15	$0.65 \pm 0.2$	$0.03 \pm 0.02$
ROLO27 (0.777 $\mu\text{m}$ )	$0.48 \pm 0.02$	$-0.3 \pm 0.04$	$0.8 \pm 0.3$	0.15	$0.55 \pm 0.2$	$0.05 \pm 0.02$
ROLO14 (0.869 $\mu\text{m}$ )	$0.51 \pm 0.04$	$-0.32 \pm 0.04$	$0.45 \pm 0.3$	0.15	$0.5 \pm 0.2$	$0.03 \pm 0.02$

The performance of the model was assessed by comparing to observations at all 11 chip locations. In this case, comparisons to the ROLO data are made both for the modeled values and the spectrally-interpolated simulated bands. These results are compiled in Appendix A and a summary is labeled as “VIS–NIR ROLO (2 component)” in Table 3. Not unexpectedly, the results for the maria and highland regions are improved relative to our initial reflectance model. For the “MareS” chip, the model is trained to an absolute

regions (e.g., “Tycho”, “TyRay”, and “Coper”) are associated with large bright craters or surrounding ejecta. Fig. 10 shows that the bright regions in the chip dataset make up a bright tail in the reflectance versus topographic height distribution as noted in Section 2.5. Therefore a third surface class, referred to as the “Crater regime”, was included to improve the performance of the model for these features. We thus defined the regime space for models M (maria), H (highlands), and C (crater) as follows:

Maria	$R_{BM} \leq 0.07$	$C_M = 1$	$C_H = 0$	$C_C = 0$
M–H Intermed.	$0.07 < R_{BM} < 0.09$	$C_M = (R_{BM} - 0.07)/0.02$	$C_H = (R_{BM} - 0.07)/0.02$	$C_C = 0$
Highlands	$0.09 \leq R_{BM} \leq 0.11$	$C_M = 0$	$C_H = 1$	$C_C = 0$
H–C Intermed.	$0.11 < R_{BM} < 0.13$	$C_M = 0$	$C_H = (R_{BM} - 0.13)/0.02$	$C_C = (R_{BM} - 0.11)/0.02$
Crater	$R_{BM} \geq 0.13$	$C_M = 0$	$C_H = 0$	$C_C = 1$

accuracy of 2.7% across all bands, while the accuracy of the spectral simulations is 3.2%. For the “Highl” chip, the accuracy of the model is 2.6% and the accuracy of the simulations is 3.5%. The performance is also good over most phase angles. The results are illustrated as residuals for the 0.747  $\mu\text{m}$  band in Fig. 9.

At other chip locations, the model accuracy, which was often greater than 10%, was not appreciably improved. Most of these

Model parameters for this third class were derived as before based on fits to the “Tycho” chip data. The scale factors  $R_{Mref} = 0.0538$ ,  $R_{Href} = 0.1042$ , and  $R_{Cref} = 0.1614$  defined in Eq. (17) represent the values of the basemap reflectance at the locations of the “MareS”, “Highl”, and “Tycho” chips that are used to train the model. The parameters for this model are summarized in Table 6.

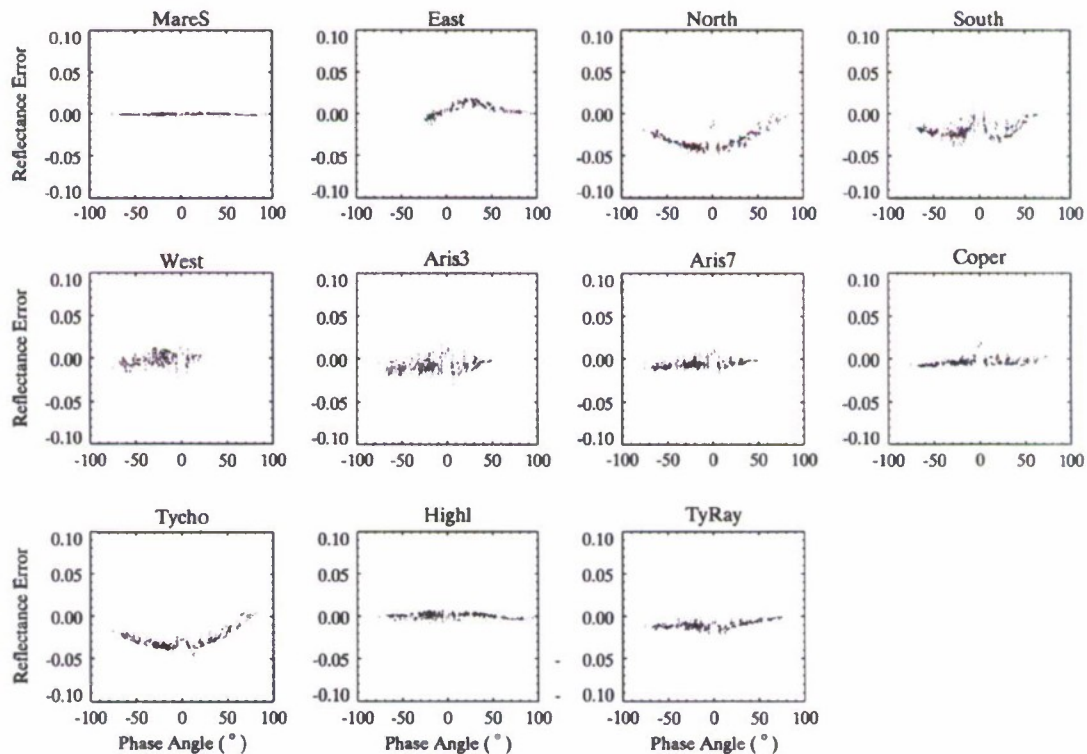


**Fig. 9.** Residuals of the two-component ROLO reflectance model minus observations. The model included maria and highland surface classes with training based on the ROLO “MareS” and “Highl” chips.

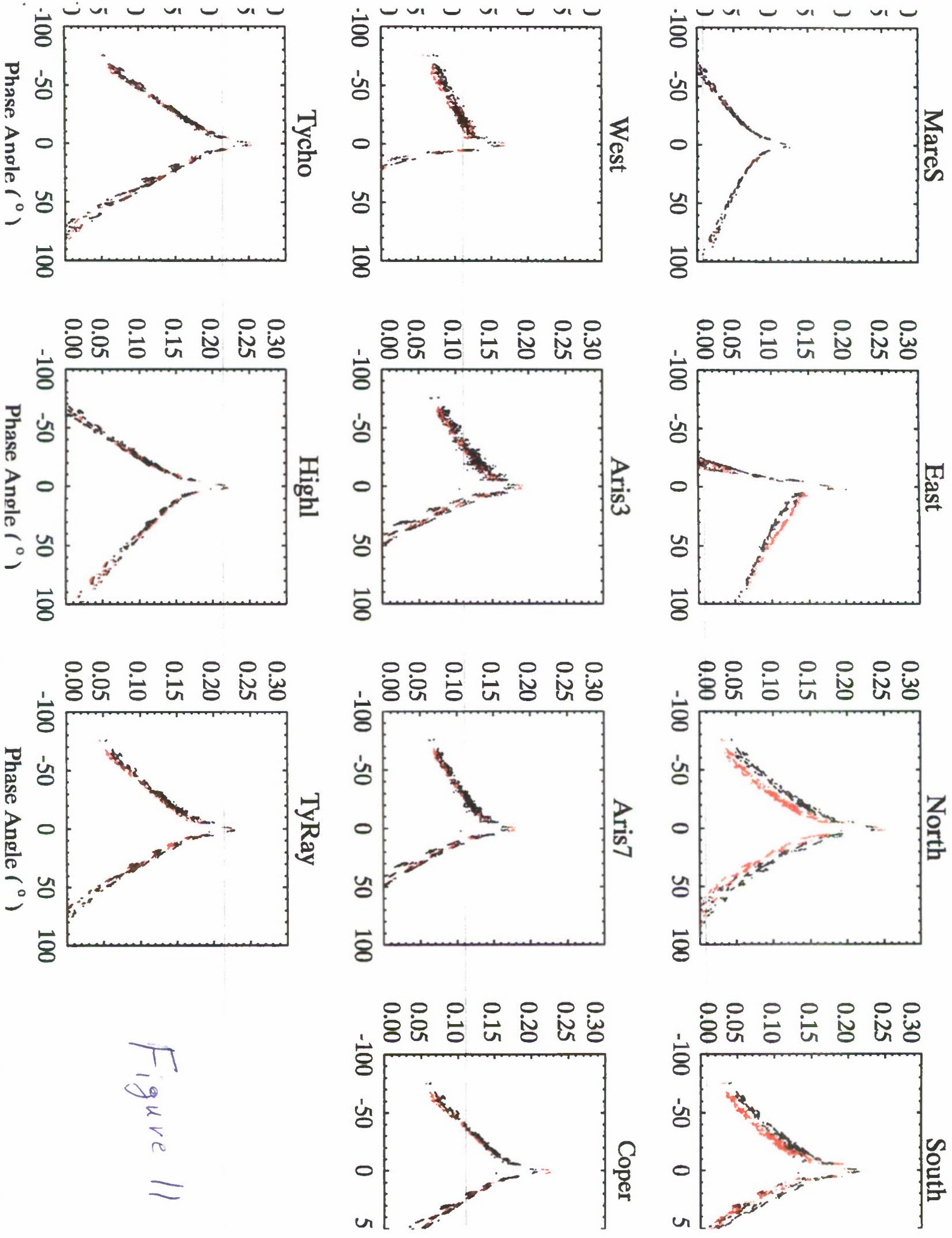
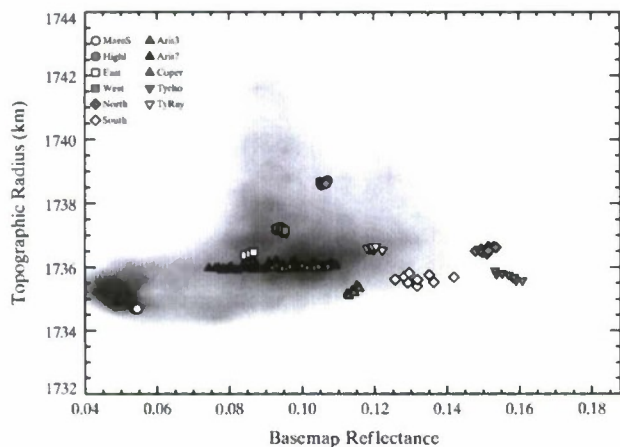


Figure 11





**Fig. 10.** Regions from the ROLO chip dataset are identified with the symbols defined in the legend in a plot of basemap reflectance versus terrain height. "MareS" and "Highl" are identified with distributions for maria and highland types while "East" and "West" represent intermediate terrain types. Values at the "North" and "South" positions are spurious due to limitations of Clementine basemap while "Aris3", "Aris7", "Coper", "Tycho", and "TyRay" represent a terrain type associated with craters. Each chip site is comprised of  $3 \times 3$  grid points (or  $7 \times 7$  for "Aris7") in the ALEX projection.

**Table 6**

Parameter solutions for the crater regime for VIS–NIR bands based on ROLO chip observations.

Band	$\bar{w}$	$g_1$	$B_0$	$h$	$B_{0c}$	$h_c$
ROLO02 (0.413 $\mu\text{m}$ )	$0.44 \pm 0.02$	$-0.3 \pm 0.05$	$0.65 \pm 0.3$	0.15	$0.4 \pm 0.2$	$0.05 \pm 0.01$
ROLO08 (0.550 $\mu\text{m}$ )	$0.54 \pm 0.02$	$-0.3 \pm 0.05$	$0.65 \pm 0.3$	0.15	$0.3 \pm 0.2$	$0.03 \pm 0.02$
ROLO10 (0.667 $\mu\text{m}$ )	$0.59 \pm 0.03$	$-0.28 \pm 0.04$	$0.7 \pm 0.3$	0.15	$0.4 \pm 0.2$	$0.02 \pm 0.01$
ROLO12 (0.747 $\mu\text{m}$ )	$0.61 \pm 0.02$	$-0.3 \pm 0.05$	$0.5 \pm 0.3$	0.15	$0.4 \pm 0.2$	$0.02 \pm 0.01$
ROLO27 (0.777 $\mu\text{m}$ )	$0.65 \pm 0.02$	$-0.3 \pm 0.05$	$0.5 \pm 0.3$	0.15	$0.4 \pm 0.2$	$0.02 \pm 0.01$
ROLO14 (0.869 $\mu\text{m}$ )	$0.65 \pm 0.04$	$-0.3 \pm 0.04$	$0.65 \pm 0.3$	0.15	$0.3 \pm 0.2$	$0.03 \pm 0.02$

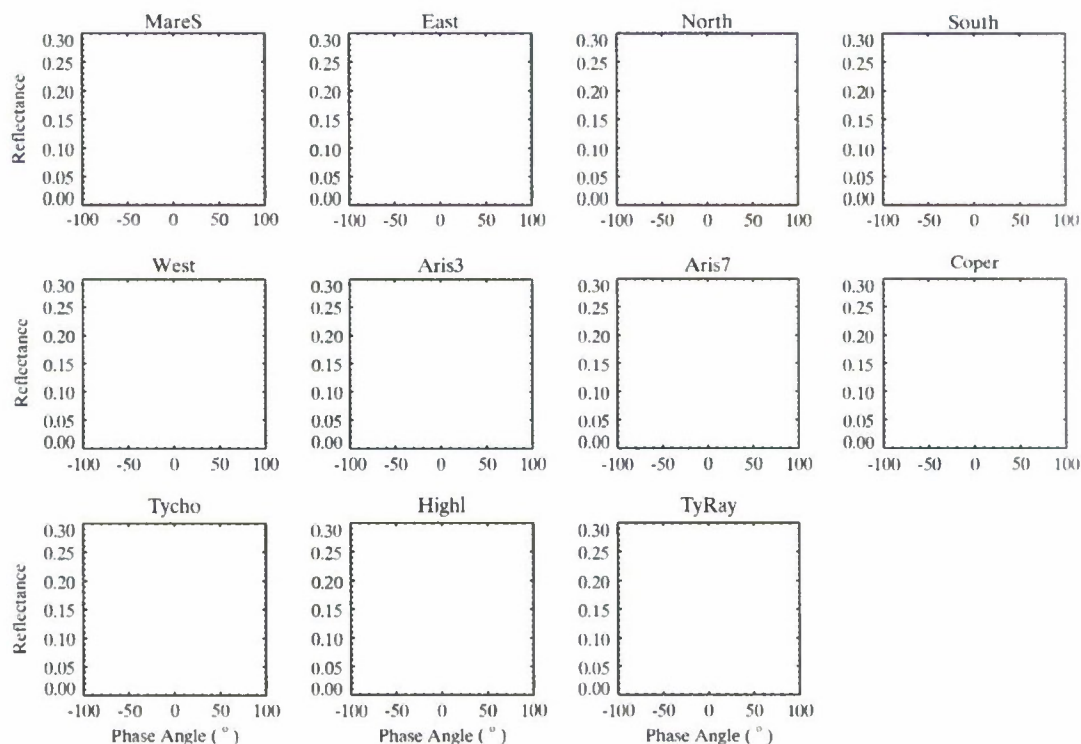


**Fig. 11.** The reflectance as a function of phase angle for the ROLO observations (black) and the three-component model (gray) for maria, highlands, and craters. Model training was based on the ROLO "MareS", "Highl", and "Tycho" chips. Color version available on-line shows the model data in red. (For interpretation of the references to color in this figure legend, the reader is referred to the web version of this article.)

The performance of this three-component model was evaluated against the ROLO chip data. The accuracy and precision for "MareS" and "Highl" are about the same as before but that for the "Coper", "Tycho", and "TyRay" chips are much improved. For "Tycho", the model and simulation accuracy are 2.6% and 1.6%, respectively. The results of this model are illustrated graphically in Figs. 11 and 12 and summarized in Table 3 under the heading "VIS–NIR ROLO (3 component)".

ROLO observations span both VIS–NIR bands (0.347–0.944  $\mu\text{m}$ ) and SWIR bands (0.944–2.390  $\mu\text{m}$ ) and the reflectance model can be extended to these data to cover the full VIS–NIR–SWIR spectrum. This is an essential analysis as attempts to extrapolate the reflectance model based on the Clementine 0.415–1.0  $\mu\text{m}$  bands to outside this range using just the Apollo 16 adjusted spectrum proved to be highly inaccurate (e.g., with errors of  $\sim 10\%$  at 1.5  $\mu\text{m}$  and  $>20\%$  at 2  $\mu\text{m}$ ). Tables 7–9 present results for the model parameters for the maria, highlands and craters, respectively, based on training to the ROLO bands 54 (1.062  $\mu\text{m}$ ), 57 (1.247  $\mu\text{m}$ ), 58 (1.543  $\mu\text{m}$ ), 60 (1.638  $\mu\text{m}$ ), and 62 (1.985  $\mu\text{m}$ ).

The SWIR model performance expressed in terms of the direct and spectrally-interpolated model bias and RMS error and are summarized in Table 3 under the heading "SWIR ROLO (3 component)" with detailed results included in Appendix A (Tables 16 and 17). The accuracy of the spectrally-interpolated simulations

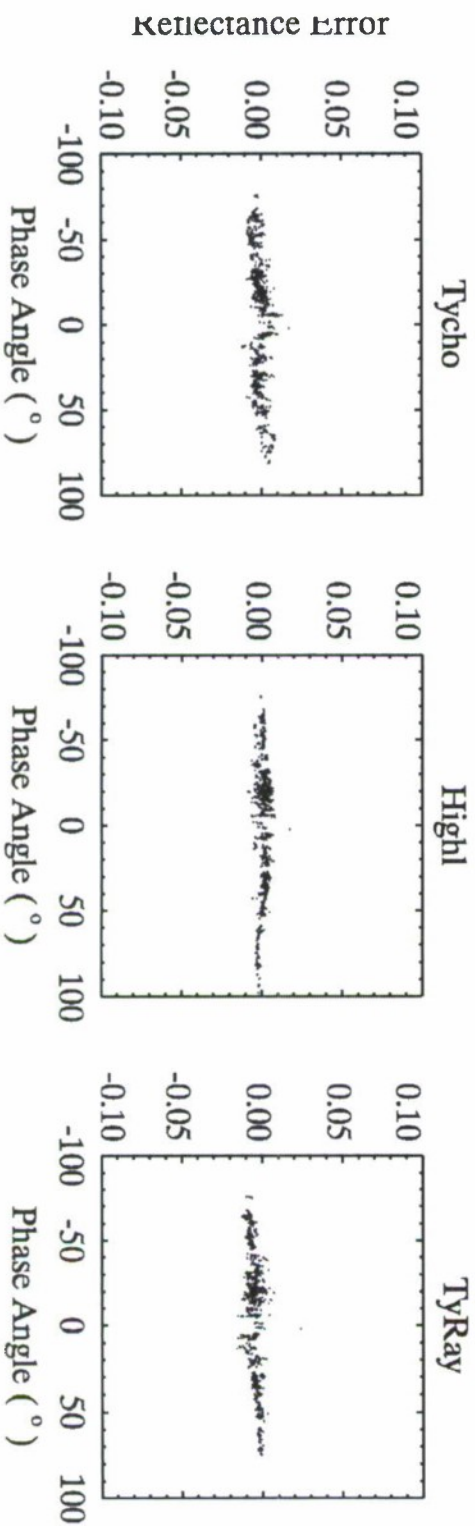
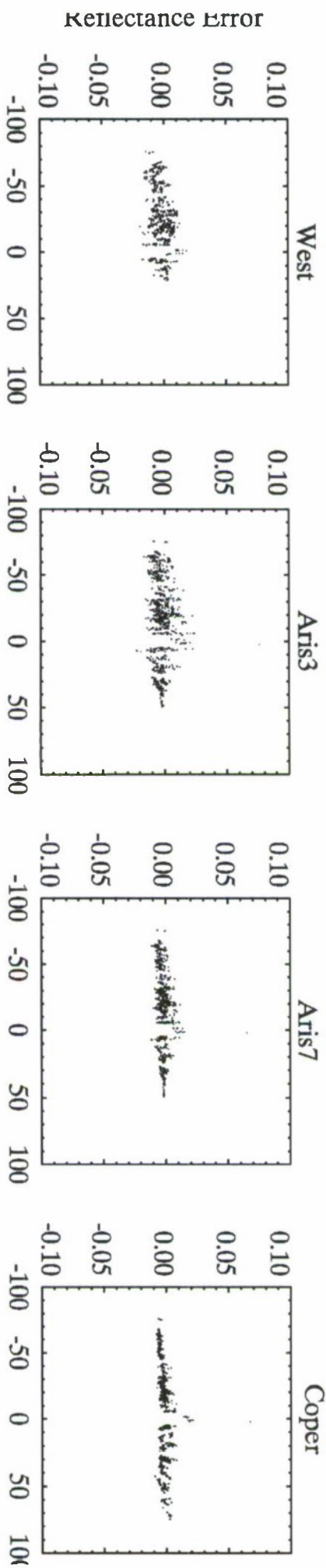
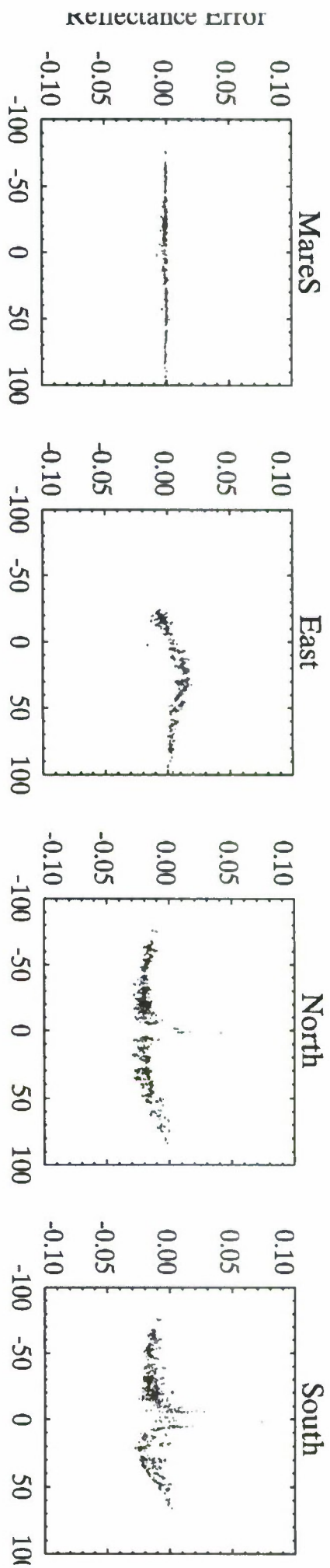
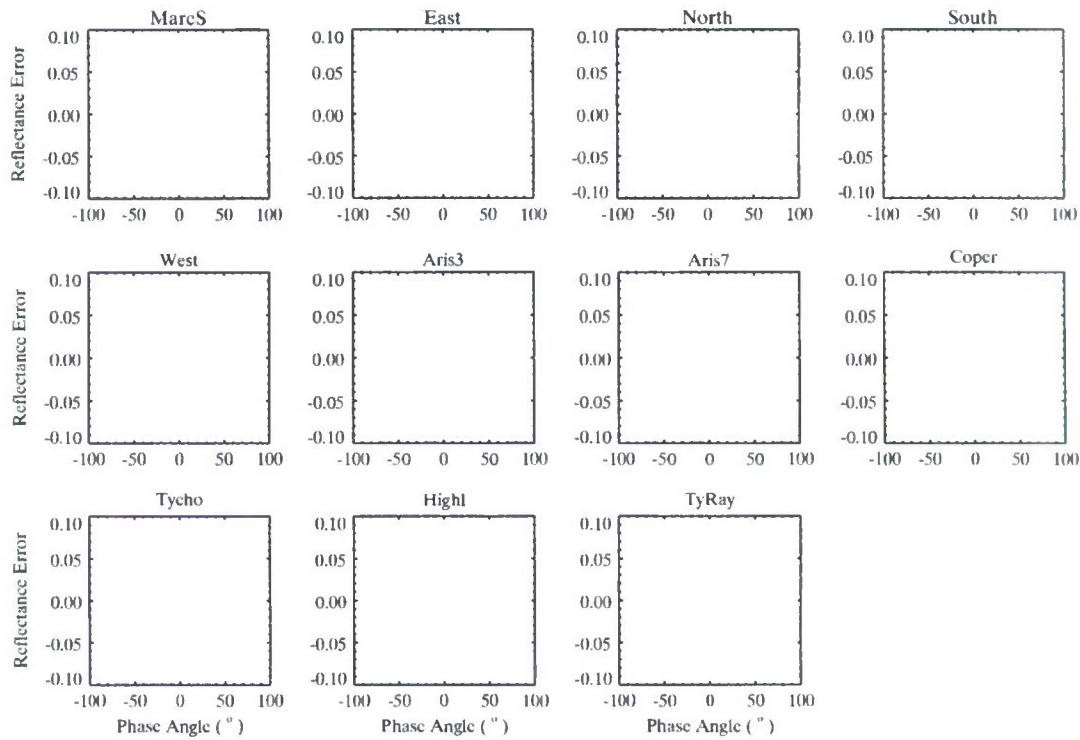


Figure 12





**Fig. 12.** Residuals between the three-component model for maria, highlands, and craters, and the ROLO Chip observations. Model training was based on the ROLO “MareS”, “Highl”, and “Tycho” chips.

**Table 7**

Parameter solutions for the maria regime for SWIR bands based on ROLO chip observations.

Band	$\varpi$	$g_l$	$B_0$	$h$	$B_{oc}$	$h_c$
ROLO54 (1.062 $\mu\text{m}$ )	$0.34 \pm 0.02$	$-0.25 \pm 0.05$	$0.8 \pm 0.3$	0.15	$0.7 \pm 0.2$	$0.11 \pm 0.02$
ROLO57 (1.247 $\mu\text{m}$ )	$0.38 \pm 0.01$	$-0.23 \pm 0.03$	$0.85 \pm 0.3$	0.15	$0.6 \pm 0.2$	$0.06 \pm 0.01$
ROLO58 (1.543 $\mu\text{m}$ )	$0.45 \pm 0.02$	$-0.24 \pm 0.05$	$0.8 \pm 0.3$	0.15	$0.5 \pm 0.2$	$0.07 \pm 0.01$
ROLO60 (1.638 $\mu\text{m}$ )	$0.47 \pm 0.02$	$-0.22 \pm 0.04$	$0.75 \pm 0.3$	0.15	$0.5 \pm 0.2$	$0.09 \pm 0.01$
ROLO62 (1.985 $\mu\text{m}$ )	$0.51 \pm 0.02$	$-0.22 \pm 0.04$	$0.75 \pm 0.3$	0.15	$0.5 \pm 0.2$	$0.09 \pm 0.02$

**Table 8**

Parameter solutions for the highlands regime for SWIR bands based on ROLO chip observations.

Band	$\varpi$	$g_l$	$B_0$	$h$	$B_{oc}$	$h_c$
ROLO54 (1.062 $\mu\text{m}$ )	$0.56 \pm 0.02$	$-0.28 \pm 0.05$	$0.7 \pm 0.3$	0.15	$0.6 \pm 0.2$	$0.06 \pm 0.01$
ROLO57 (1.247 $\mu\text{m}$ )	$0.59 \pm 0.02$	$-0.28 \pm 0.05$	$0.45 \pm 0.3$	0.15	$0.6 \pm 0.2$	$0.05 \pm 0.01$
ROLO58 (1.543 $\mu\text{m}$ )	$0.66 \pm 0.02$	$-0.28 \pm 0.05$	$0.7 \pm 0.3$	0.15	$0.5 \pm 0.2$	$0.04 \pm 0.01$
ROLO60 (1.638 $\mu\text{m}$ )	$0.67 \pm 0.02$	$-0.25 \pm 0.05$	$0.5 \pm 0.3$	0.15	$0.45 \pm 0.2$	$0.05 \pm 0.01$
ROLO62 (1.985 $\mu\text{m}$ )	$0.71 \pm 0.02$	$-0.25 \pm 0.05$	$0.7 \pm 0.3$	0.15	$0.4 \pm 0.2$	$0.05 \pm 0.02$

**Table 9**

Parameter solutions for the crater regime for SWIR bands based on ROLO chip observations.

Band	$\varpi$	$g_l$	$B_0$	$h$	$B_{oc}$	$h_c$
ROLO54 (1.062 $\mu\text{m}$ )	$0.68 \pm 0.02$	$-0.25 \pm 0.05$	$0.65 \pm 0.3$	0.15	$0.4 \pm 0.2$	$0.04 \pm 0.02$
ROLO57 (1.247 $\mu\text{m}$ )	$0.71 \pm 0.02$	$-0.3 \pm 0.05$	$0.45 \pm 0.3$	0.15	$0.4 \pm 0.2$	$0.03 \pm 0.02$
ROLO58 (1.543 $\mu\text{m}$ )	$0.76 \pm 0.02$	$-0.25 \pm 0.05$	$0.65 \pm 0.3$	0.15	$0.4 \pm 0.2$	$0.03 \pm 0.02$
ROLO60 (1.638 $\mu\text{m}$ )	$0.78 \pm 0.02$	$-0.25 \pm 0.05$	$0.65 \pm 0.3$	0.15	$0.4 \pm 0.2$	$0.05 \pm 0.02$
ROLO62 (1.985 $\mu\text{m}$ )	$0.8 \pm 0.02$	$-0.25 \pm 0.05$	$0.65 \pm 0.3$	0.15	$0.3 \pm 0.2$	$0.06 \pm 0.04$

depended on the bands used to fit the spectrum. This was especially the case for the SWIR bands, where it was important to include a subset of the NIR bands in the model fit. For example, including band 27 (0.777  $\mu\text{m}$ ) in the model fit improved simulated reflectance accuracy at the shortest-wavelength modeled SWIR band (1.062  $\mu\text{m}$ ).

Thermal emission accounts for a perceptible amount of the measured radiance in the longest ROLO SWIR bands at 2.256 and 2.390  $\mu\text{m}$ . Assuming a sub-solar temperature of 395 K, a  $\cos^{1/4} i$  ( $i$  = incidence angle) temperature distribution, and an emissivity of 1.0, it is straightforward to calculate that thermal component contributes between 5% and 8% of the measured signal in the

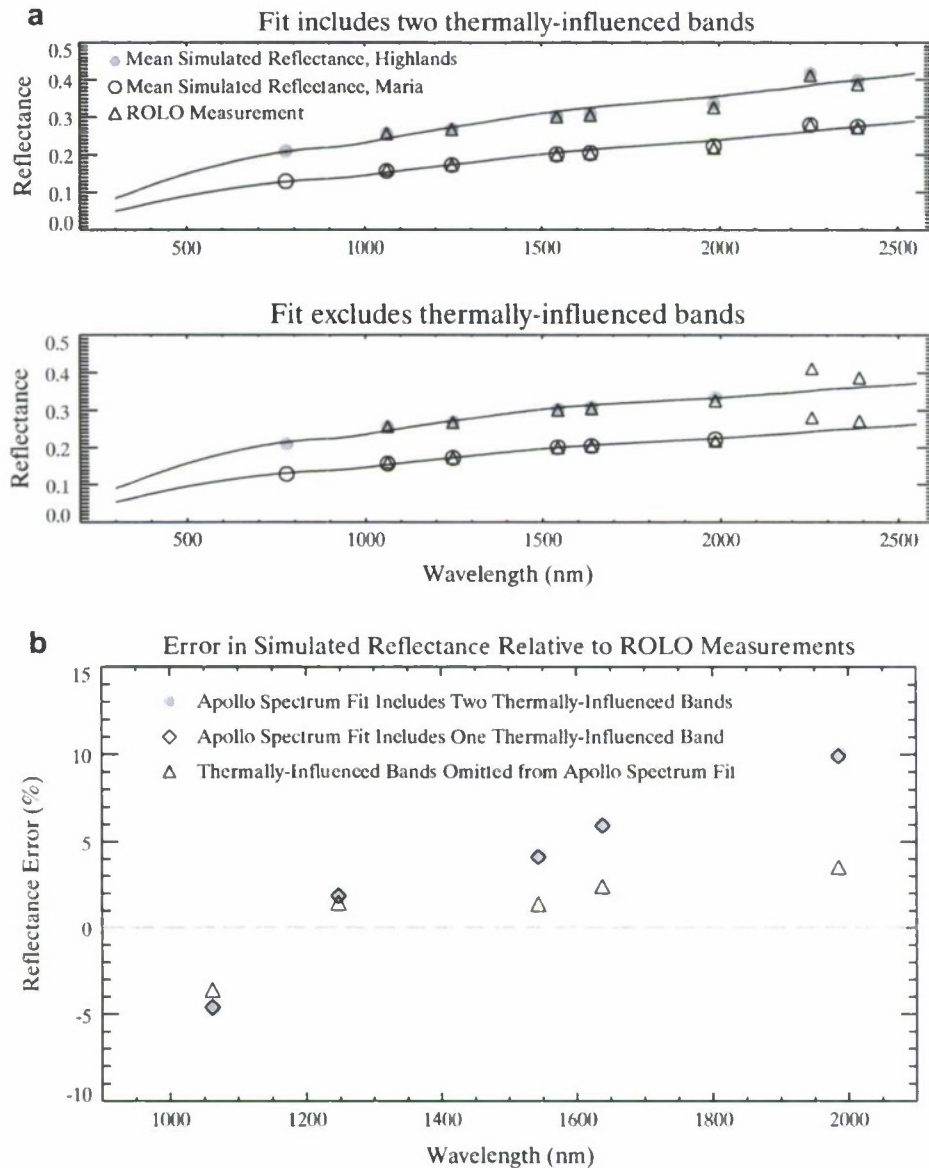


**Fig. 13.** Fraction of lunar signal attributable to thermal emission for ROLO SWIR passbands, plotted as a function of distance from the sub-solar point. The thermal contribution was computed from the Planck function assuming a 395 K sub-solar surface temperature. The temperature at a location was scaled by a factor of  $\cos^{1/4} \theta$ , where  $\theta$  is the angular separation from the sub-solar point (i.e. the sub-solar colatitude). Reflectance error of the spectrally-interpolated simulation results relative to corresponding ROLO measurements. The accuracy of the fitted Apollo spectrum is sensitive to the choice of NIR bands used to perform the fitting. (a) Measured and simulated reflectance spectra for highland and maria surface regimes (indicated by triangles and circles). The scaled Apollo 16 soil reflectance spectra are computed for maria and highland and superimposed. The second panel demonstrates the improved accuracy in the fitted Apollo spectrum that results from omitting the two longest-wavelength ROLO bands from the fit. (b) The percent error in the simulated reflectance for the combined maria and highland surface regimes.

2.39  $\mu\text{m}$  band for the nearly full Moon. Thermal emission contributes up to 2–3% of the signal at 2.26  $\mu\text{m}$ , and the thermal component rapidly diminishes at shorter wavelengths. Since the laboratory-measured Apollo 16 spectrum accounts for reflectance only, attempts to scale the spectrum using thermally-contaminated bands would result in erroneous fits across a broad region of the near IR and shortwave IR spectra. This is illustrated in Fig. 13, in which the reflectance is simulated for the observation time 2 March 1999 at 04:50 UT. The accuracy of the simulated reflectance improves when the long wavelength ROLO bands are omitted from the Apollo soil spectrum fit.

The relative contribution of shadow-hiding and coherent backscatter to the opposition surge has been much discussed in the literature (e.g., Buratti et al., 1996; Helfenstein et al., 1997; Hillier

et al., 1999; Hapke, 2002). Previous analysis indicated that the opposition surge is represented by a broad peak that is associated with shadow-hiding and a narrow peak that is due to coherent backscatter. This is consistent with the solution derived in this paper (i.e.,  $\Delta\alpha_{\text{SH}} = 17^\circ$  and  $\Delta\alpha_{\text{CB}} < 5^\circ$ ). The predicted behavior as a function of albedo and wavelength has been used to argue for the relative importance of shadow-hiding and coherent backscatter to the lunar opposition effect. For example, Hillier et al. (1999) discussed their results based on models for the maria and highlands derived from Clementine 0.4 – 1.0  $\mu\text{m}$  data. The model parameters from our solution are presented in Fig. 14 as a function of wavelength for the complete set of ROLO wavebands (0.4–2.4  $\mu\text{m}$ ). Essential deductions from our solution in the context of the predictions from scattering theory are:



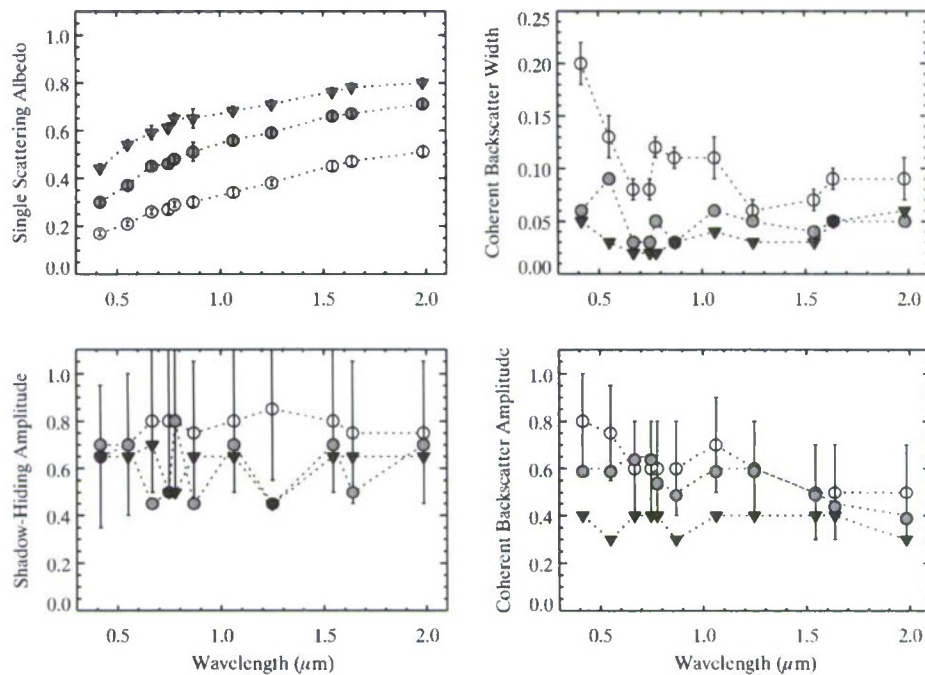


**Fig. 14.** Solutions in the ROLO bands for the free parameters in the scattering model. The solutions for the maria (white circles), highlands (gray circles), and craters (black triangles) are shown. The single scattering albedo increases with wavelength. Other model parameters show considerable variation from channel to channel. The shadow-hiding width is fixed at 0.15 and the amplitudes are constant but with large scatter. The coherent-backscatter width is greatest for the maria and the amplitude tends to decrease with wavelength. Except for the single scattering albedo, error bars are shown for only for the maria to avoid cluttering the plots; uncertainties for all parameters are included in Tables 4–9.

- Prediction: The shadow-hiding width is independent of wavelength. This is a consequence of shadowing-hiding being a geometrical effect governed by the porosity of the medium with grain sizes much larger than the wavelength of light. The increase in intensity at opposition results from light rays scattered off surfaces near the entry point back towards the source. Our analysis indicated no evidence for a wavelength dependence and a solution was adopted that fixed the shadow-hiding width to a constant value, i.e.,  $h = 0.15$  or  $\Delta\alpha_{SH} = 17^\circ$ . This value was found to be suitable for all surface classes (maria, highlands, and crater). The shadow-hiding widths derived by Hillier et al. (1999), with means equal to  $5.7^\circ$  (maria) and  $6.7^\circ$  (highlands), were also reported to be independent of wavelength.
- Prediction: Coherent-backscatter width is proportional to wavelength. Coherent backscatter near zero phase angle arises as a result of constructive interference associated with light waves that undergo multiple scattering from particles with sizes that are comparable to the wavelength of light. The Hillier et al. (1999) results for maria and highlands revealed no dependence of the coherent-backscatter width on wavelength. Similarly, within a surface class, we find no evidence for the coherent-backscatter width to vary with wavelength. Hapke et al. (1993) suggested this could be explained with the presence of a wide size distribution of the scattering particles.
- Prediction: Coherent-backscatter width is inversely proportional to albedo. Coherent-backscatter width is inversely proportional to the mean photon optical path that, for multiple scattering, increases as the albedo is increased. In our derivation, the coherent-backscatter width is greatest for the maria and is consistent with this prediction. This is also supported by the results of Hillier et al. (1999).
- Prediction: Shadow-hiding amplitude decreases with albedo. Helfenstein et al. (1997) proposed that low-albedo grains are more opaque than high-albedo grains such that the relative

contribution from single scattered reflections would be greater for darker surfaces. Hillier et al. (1999) reported model results that appeared to substantiate this prediction. However, in our analysis, we find the uncertainties in the derived amplitudes to be too large to be conclusive.

- Prediction: The coherent-backscatter amplitude increases with albedo. The albedo increases with wavelength but in our model the coherent-backscatter amplitude dependence on wavelength (i.e., albedo) is flat or decreases slightly and there is no clear separation between amplitude for maria, highlands, or crater regions. This result is consistent with the findings of Hillier et al. (1999), though in their results, they found that the amplitude associated with the maria was smaller than that for the highlands. Again, in our analysis the uncertainties in the derived amplitudes are too large to be conclusive.

Thus we find that some but not all predictions are supported by our model derivation. Given the uncertainty owing to the non-uniqueness of the solution, an assessment of the relative contributions of shadow-hiding and coherent backscatter may be difficult to resolve. Our solution was derived independently for each waveband. Specific models could be investigated by enforcing constraints on the model parameters with wavelength and albedo.

### 3.3. Model development and analysis based on ROLO images

#### 3.3.1. Analysis of the disk-resolved reflectance

The final step in developing the reflectance model was to compare the three-component model predictions with ROLO image observations and adjust the model parameters to fit the observations. The comparison also resulted in minor corrections to the basemap itself. The imagery used in this analysis was obtained on 02 March 99 and 03 March 99 when the Moon was nearly full (i.e., phase angles  $<15^\circ$ ). The calibration of this imagery is based

on the updated results of Kieffer and Stone (2005) using Vega as a calibration source and is consistent with that used for the ROLO Chip dataset. (Note that Engelke et al. (2010) and references therein comment that Vega is episodically variable by several percent.) The three-component (maria, highlands and craters) regime model described in Section 3.2.2 is used to compute full disk reflectance for the times of observation and the performance is reported in terms of accuracy and precision by surface class. Using the classification criteria defined above, the lunar surface is classified as 33% maria, 20% intermediate maria/highlands, 27% highlands, 15% intermediate highlands/crater, and 6% crater (excluding areas of bad or missing data).

Initial attempts to model the ROLO image data uncovered two issues. First systematic reflectance errors were present within each of the regime ranges. In other words, within the range of a specified reflectance regime (e.g., maria), the reflectance could not be simply represented as the model reflectance scaled by the basemap reflectance as specified in Section 3.2.1 for the three-component model. The lunar reflectance had a more complex dependency on surface albedo than originally assumed. However, it was found that this dependence could be modeled by modifying Eq. (17) as follows.

Maria-highlands	$R_{BM} \leq R_{REF,H}$	$C_M = (R_{BM} - R_{REF,M}) / (R_{REF,H} - R_{REF,M})$
Highlands-crater	$R_{BM} > R_{REF,H}$	$C_M = 0$

In other words, the reflectance for maria through highlands could be modeled as a weighted sum of the maria and highlands models and the reflectance for highlands through crater could be modeled as a weighted sum of the highlands and crater models. This approach has the rather unsatisfactory characteristic, though, that  $C_M < 0$  and  $C_H > 1$  when  $R_{BM} < R_{REF,M}$  and  $C_C < 0$  and  $C_H > 1$  when  $R_{BM} > R_{REF,C}$ .

The second problem was that a discernable bias in reflectance error was detected between the East and West portions of the Moon. We ascribed this error to the basemap (i.e., a consequence of the Clementine mosaic process) rather than the ROLO observations, which imaged the entire Moon at a given time on the CCD. We found that a linear adjustment to the Clementine basemap reflectances corrects this problem (detailed in Appendix B). The correction changes the reflection by, at most,  $\pm 9\%$  near the limb. This correction may be considered to be a refinement to the scaling

factor that Hillier et al. (1999) introduced to make the Clementine data match historical observations.

The model results are illustrated by the pair of images in Fig. 15 showing the observed and modeled lunar image at  $0.747 \mu\text{m}$  from 02 March 1999 04:53 UT. The modeled reflectances were simulated at nominal resolution and then convolved with a point-spread function to approximate the spatial resolution of the ROLO observations and finally resampled to the ALEX projection. Visually, the images agree quite well. This simulated imagery includes the correction to the basemap to account for missing data and striping described in Appendix B (i.e., the basemap has been corrected using the ROLO imagery as a reference).

A scatter plot of the reflectance error versus basemap reflectance is shown in Fig. 16 for this image. In this plot, the limits for the maria, highlands and crater regimes are identified and the reflectance errors for the "MareS", "Highl", and "Tycho" chips are also indicated. Note that regions where data was missing from the original basemap have not been included in the performance analysis. The performance results for VIS–NIR bands are summarized in Table 10 with details presented in Table 18 (for the direct model predictions) and Table 19 (for the spectrally-interpolated model predictions). The model bias derived from the imagery is

$C_H = (R_{REF,H} - R_{BM}) / (R_{REF,H} - R_{REF,M})$	$C_C = 0$
$C_H = (R_{BM} - R_{REF,H}) / (R_{REF,C} - R_{REF,H})$	$C_C = (R_{REF,C} - R_{BM}) / (R_{REF,C} - R_{REF,H})$

typically 2–3% for the VIS–NIR bands. Table 10 also includes the summarized performance results for the SWIR bands, with detailed results provided in Tables 20 and 21. The SWIR band bias is below approximately 4% for the various surface classes.

### 3.3.2. Analysis of the disk-integrated reflectance

The final comparison we make is to the disk-integrated reflectance. For this exercise we compute three quantities: first, the observed reflectance derived directly from the ROLO imagery (in the ALEX projection), second, the predicted reflectance based on the empirical formula of Kieffer and Stone (2005) (i.e., Eq. (1)), and third, the disk-integrated reflectance derived from the simulated ROLO image. The model reflectance was computed as described above: generating the image in the observer projection convolved with the instrument response function, then resampled to the ALEX projection. The integrated reflectance was computed as the

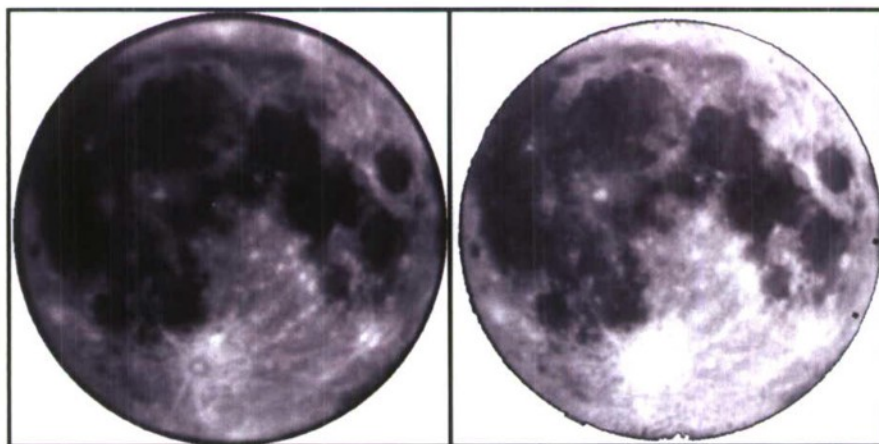
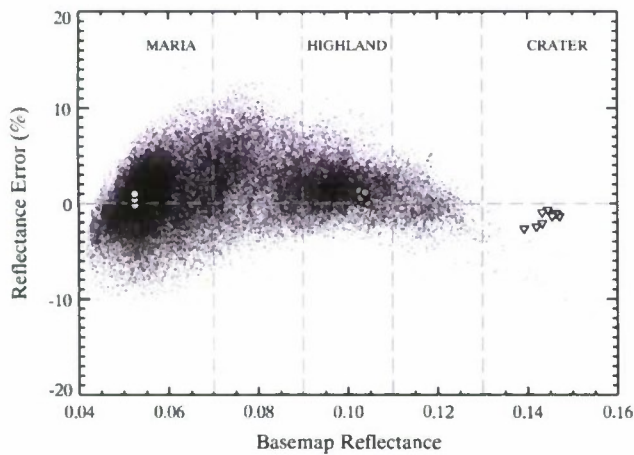


Fig. 15. Comparison of the observed ROLO image at  $0.747 \mu\text{m}$  from 02 March 99 04:53 UT (left) with the modeled image (right). The simulated image is based on a basemap that includes corrections for holes and striping that are present in the original Clementine basemap (see Appendix B).





**Fig. 16.** Scatter plot showing reflectance error in percent as a function of the basemap reflectance for 0.747  $\mu\text{m}$  ROLO observations on 02 March 99 at 04:53 UT. Limits for maria (<0.07), highlands (0.09–0.11), and crater (>0.13) are indicated by dashed lines. The errors associated with points corresponding to the “MareS”, “Highl”, and “Tycho” chips are indicated as white circles, gray circles, and white triangles, respectively.

**Table 10**  
Performance summary for VIS–NIR and SWIR bands from analysis of ROLO imagery.

Chip	Bias (%) <sup>a</sup>	RMS (%)
VIS–NIR (0.413, 0.550, 0.667, 0.747, 0.868 $\mu\text{m}$ )		
Maria	3.7 (2.7)	4.1
Highland	2.4 (2.4)	2.8
Crater	2.3 (2.5)	3.0
Overall	3.0 (2.5)	4.4
Disk integrated	2.8 (1.5)	1.3
SWIR (1.062, 1.247, 1.543, 1.638, 1.985 $\mu\text{m}$ )		
Maria	4.1 (2.9)	3.6
Highland	3.5 (2.9)	2.9
Crater	2.7 (1.5)	2.7
Overall	3.2 (2.2)	4.2
Disk integrated	2.0 (1.5)	1.8

<sup>a</sup> Error from direct model calculation in is parentheses.

average reflectance for all valid points on the simulated image. The results are illustrated in Fig. 17 for the 02 March 1999 and 03 March 1999 ROLO observations. From this figure it is apparent that the accuracy of the modeled disk-integrated reflectance is comparable to that derived using the empirical formula. For the VIS–NIR bands we find the accuracy of the model is 1.5% (from the direct calculation) and 2.8% (from the spectrally-interpolated calculation). The RMS error is found to be 1.3%. Similar performance was noted in the SWIR bands. Results are summarized in Table 10.

#### 4. Discussion

We adopted a five term analytic scattering function to represent the reflectance of the Moon: a two term Henyey–Greenstein single scattering function, a multiple scattering function with a first order Legendre polynomial to represent the asymmetry, shadowing and coherent backscatter expression for the opposition surge and a shadowing expression. Many have noted that the parameters in the scattering functions are strongly coupled. Specific examples include the following.

##### 4.1. Photometric roughness angle

Hapke (1984) derived expressions for the photometric roughness in which a tilt angle parameterizes the effects of macroscopic roughness in his photometric model. This parameter accounts for the effects of sub-resolution scale roughness, which may be important on sub-millimeter to kilometer scales. The analysis of Goguen et al. (2010) confirmed earlier results in determining that the roughness tilt angle is sensitive to 0.1–1 mm size scales for maria and highland surfaces. This demonstrates that photometric measurements respond to roughness at the level of micro-topography, rather than at the scale of more familiar topographic features such as crater ridges and hills.

Past studies (Helfenstein et al., 1997; Hillier et al., 1999; Goguen et al., 2010) independently derived tilt roughness angles in the range of approximately 20–35° for lunar maria and highland regions, with larger roughness associated with the highlands. Given the strong support in the literature for these scales, we adopted roughness angles of 24° for the maria and 27° for the highlands,

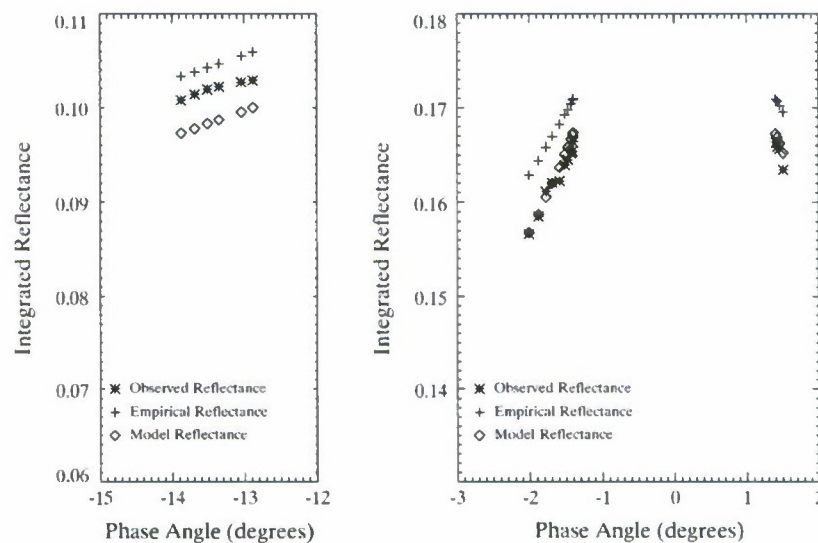


**Fig. 17.** Comparison of disk-integrated reflectance at 0.747  $\mu\text{m}$  based on the ROLO observations, the empirical model from Kieffer and Stone (2005), and that computed from the reflectance model.



as did Hillier et al. and also adopted the  $27^\circ$  tilt angle to the crater regime in our model. Assuming fixed values for the tilt angle reduces the number of free parameters in the Hapke model and mitigates, at least in part, the uncertainty due to the non-uniqueness of the solution. Shepard and Helfenstein (2007) noted a weak correlation between the roughness tilt angle and the shadow-hiding angular width, suggesting a physical link between these two phenomena, which is reflected in the larger value of the brighter highlands. This finding further underscores the potential coupling between these two terms as a basis for adopting Hillier's roughness angles rather than directly fitting to the observations.

Goguen et al. (2010) showed the Hapke shadowing formulation and multiple scattering have similar photometric signatures, which demonstrates the potential for additional coupling among model parameters. Goguen et al. successfully fit the ROLO observations using both a single scattering model with (1) a relatively rough surface (roughness tilt angle of  $34^\circ$  for highlands), and with (2) a multiple scattering model assuming a photometrically smooth surface. This finding highlights the ambiguity between the two terms, as the relative contributions of roughness and multiple scattering are not well-constrained.

#### 4.2. Single scattering albedo

Our fits unambiguously show that the single scattering albedo has a strong spectral dependence, increasing with wavelength in agreement with existing observational evidence. Furthermore, our fits to single scattering albedo are robust with uncertainties of typically  $\pm 0.03$  or less. However, Shepard and Helfenstein (2007), who fit the Hapke model to laboratory bidirectional reflectance measurements of various soil samples, showed that the single scattering albedo depends on soil packing state. This result was unexpected given that the single scattering albedo is a property of an individual scatterer, and should not depend on whether a soil sample is loose grained or compacted. This dependency was attributed to the fact that soil porosity was not treated in the Hapke model. Although the model has since been revised to account for porosity outside of the opposition effect (Hapke, 2008), which consists of multiplying Eq. (4) by a constant derived from the fill factor of the particles and modifying the  $H$  terms with this factor, we did not adopt this formulation, in the present study. We thus recognize that our derived single scattering albedo is sensitive to regolith packing state rather than being diagnostic of the component particles. Without treatment of porosity, the single scattering albedo may be sensitive to the size distribution of particles in the scattering medium. Hapke (2008) explains that reflectance is sensitive to particle filling factor (i.e. the degree to which small grains pack the interstices between larger particles) as reflectance first increases with filling factor, reaches a maximum, and then decreases for highly dense soils. Thus, while our derived single scattering albedo exhibits the expected trends, stronger constraints might be imposed by accounting for the effects of porosity.

#### 4.3. Shadow-hiding and coherent backscatter

Since albedo is proportional to wavelength, it may be hypothesized that the shadow-hiding and coherent backscatter terms have varying levels of importance depending on the spectral region. A reduction in multiple scattering is expected at short wavelengths as the surface is more absorbing. At large viewing angles, shadows therefore do not experience illumination from multiply scattered photons. When the surface is viewed at a low phase angle, a strong surge would occur as the shadows become hidden and the surface brightens. At longer wavelengths, the surface albedo is higher and the increased multiple scattering partially illuminates the primary shadows. When the surface is viewed at low phase angles, the ob-

served surge would be the result of the multiply scattered photons producing a coherent backscatter effect.

However, the analysis of Clementine visible and near-IR data by Buratti et al. (1996) did not identify spectral trends in the opposition surge. They concluded that shadow-hiding was the dominant opposition surge mechanism given the lack of an increased surge at longer wavelengths. This finding was supported by the results of Shepard and Helfenstein (2007), whose laboratory measurements (confined to phase angles  $>3^\circ$ ) identified that the surge width was relatively constant with wavelength.

The ROLO observations examined in the present study cannot separate the relative importance of shadow-hiding and coherent backscatter, or further verify whether shadow-hiding is the dominant phenomenon, as suggested above. While the lack of coverage at phase angles below approximately  $1.5^\circ$  is a limiting factor, a greater concern is the strong coupling between the two terms. Our attempts to simultaneously fit shadow-hiding and coherent backscatter reveal the lack of constraint as the non-unique solutions compensate for one another with little basis in physical realism; this lack of constraint has been encountered in past studies (e.g. Shepard and Helfenstein, 2007). Nelson et al. (2000) and Hapke (2002) propose that circularly polarized observations may be required to adequately constrain the opposition surge.

### 5. Conclusions

The model developed in this article computes the lunar reflectance and disk-resolved radiance of the entire Moon using the physics-based scattering formulation of Hapke to scale the Clementine basemap. In contrast to previous scattering models, we have explicitly modified the direction cosines for the incident and emergent directions using the normal to a surface element as specified by the recently available high resolution (2 km) lunar topographic map. We initially constructed a reflectance model to match the results of Hillier et al. (1999) for the Clementine bands. This model was able to reproduce the predictions of Hillier et al. albeit with slightly different parameters. The most discrepant parameter was the width of the shadow-hiding contribution to the opposition surge, which was generally about  $2\frac{1}{2}$  times larger than that found by Hillier et al., though this parameter is shown to be poorly constrained.

We improved the accuracy of the reflectance predictions by training the model against the ROLO chips representative of the maria (labeled MareS) and highland (HighL), by introducing a third terrain type identified with bright craters and trained based on the ROLO Tycho chip, and by allowing mixing between the three terrain types. The performance of this model was evaluated by comparison to the complete ROLO chip dataset and to a sample of the ROLO imagery near full Moon. The final model was extended to the shortwave IR (0.35–2.45  $\mu\text{m}$ ) and is able to reproduce the ROLO observations within a day of full Moon within an RMS scatter of  $\sim 3\%$  at all visible and short wavelength infrared.

The ROLO chip data provide reflectivity as a function of phase for 11 separate locations on the Moon in 32 narrow spectral bands between 0.35 and 2.45  $\mu\text{m}$ . Thus, we have derived model parameters for each of these 32 bands in addition to the five Clementine bands represented by the Hillier et al. models. However, since a primary motivation in creating this model was to provide a method by which the (nearly) full Moon may be used as a calibration resource for Earth resource satellites, the reflectance for any defined spectral bandpass can be computed by fitting a scaled  $(a + b\lambda)$  spectrum of Apollo 16 soil sample through the reflectivities for the model bandpasses. Though the spectral interpolation induces some error, we explicitly address this contribution in the performance estimates presented throughout the paper.



In addition, the model also can be used to calculate disk-integrated reflectance. To derive radiance or irradiance the respective reflectance is multiplied by the incident solar flux from a Kurucz solar model. Furthermore, the spatial sampling, spatial response and spectral response functions may be a user-defined input, which permits direct comparison between the model and systems other than ROLO.

Recently, the demonstration of strong coupling among the derived parameters led Shepard and Helfenstein (2007) to conclude (we paraphrase) that the Hapke scattering model (represented by Eq. (4)) was not a reliable remote sensing tool to derive the physical properties of the Moon and that the model parameters represent complex combinations of particulate properties, surface roughness, and packing. Our approach was not to attempt to infer surface properties by restricting the observations to limited phase angles, such as near opposition, but to develop a global model to account for observations of the Moon within a day of opposition based on the disk resolved Clementine and ROLO observations. We report uncertainties in the derived model parameters, many of which are not well-constrained and this analysis supports the conclusions of Shepard and Helfenstein.

Further extensions and improvements to the model are planned. These include modeling of shadowing casting caused by surface features in order to improve the fidelity of the predicted reflectance near the terminator at larger phase angle. While topography is included in the model and is used to determine the incidence and emittance angles at the surface, the current model does not account for shadowing or obscuration resulting from the surface topography. The errors introduced by not including shadow casting are small if the model is applied to the Moon near full or the region of interest is well away from the terminator. However, shadow

casting and topography, through the hemispherical reflectance (e.g. Lawson and Jakosky, 2001), will be important to extend the modeling into the thermal infrared. The next significant upgrade is to model the disk-resolved thermal emission from the Moon.

### Acknowledgments

We thank Tom Stone and Hugh Kieffer for providing the ROLO data and for useful discussions regarding the interpretation of the data and the reflectance model. Paul Noah performed the initial steps in the development of the model software. This work was funded by the National Geospatial Intelligence Agency. This work made use of NASA's Astrophysics Data System Bibliographic Services. The Map-a-Planet project and web site is maintained by the USGS Astrogeology Research Program, <http://astrogeology.usgs.gov>; the material is based upon work supported by NASA.

### Appendix A. Model performance analysis

The detailed performance results from the various stages of model development expressed as percent bias and RMS are summarized in Tables 11–21. The initial model was fit to the Hillier et al. model predictions for the Clementine bands. Table 11 shows results of the spectrally-interpolated model predictions with ROLO chip data. At 0.747  $\mu\text{m}$ , the accuracy for the “MareS” chip is 2.6% and for the “Highl” chip is 4.5%, but the model errors are larger for other wavebands. At other chip locations, the accuracy is also significantly limited. As a result, while this model provides reasonable general agreement with the ROLO observations, the performance is insufficient as a tool for calibration.

**Table 11**  
Evaluation of the spectrally-interpolated model predictions with ROLO chip data in VIS–NIR bands based on the two-component Clementine model solution.

Chip	ROLO02 (0.413 $\mu\text{m}$ )		ROLO08 (0.550 $\mu\text{m}$ )		ROLO10 (0.667 $\mu\text{m}$ )		ROLO12 (0.747 $\mu\text{m}$ )		ROLO14 (0.868 $\mu\text{m}$ )	
	Bias	RMS	Bias	RMS	Bias	RMS	Bias	RMS	Bias	RMS
1. MareS	7.6	2.1	8.4	2.2	–4.1	2.2	–2.6	2.3	–8.1	1.7
2. East	11.8	5.1	13.9	4.4	0.2	4.8	2.7	5.0	–6.7	4.4
3. North	–0.3	15.3	0.6	15.7	–7.6	15.0	–4.2	15.4	–7.9	14.7
4. South	–11.6	21.8	–15.9	26.3	–19.4	23.3	–15.5	25.3	–23.2	22.3
5. West	5.7	5.4	18.2	5.3	–0.5	5.3	3.3	6.1	–8.4	4.7
6. Aris3	8.3	14.7	–1.2	13.1	9.6	14.3	18.4	15.5	18.9	13.8
7. Aris7	5.6	8.9	4.1	7.9	6.2	8.3	13.8	9.2	12.1	8.1
8. Coper	5.8	5.3	4.3	5.8	–1.5	5.2	3.1	5.5	–3.7	4.2
9. Tycho	4.6	18.7	6.8	18.3	4.6	16.7	9.6	17.0	4.9	3.3
10. Highl	7.1	3.9	11.3	3.7	1.8	4.1	4.5	4.0	–5.0	3.3
11. TyRay	9.8	4.6	6.2	4.9	4.7	4.9	9.7	5.0	2.4	3.9

**Table 12**  
Bias and RMS between direct model predictions with ROLO chip data in VIS–NIR bands based on the ROLO two-regime (maria, highlands) model solution.

Chip	ROLO02 (0.413 $\mu\text{m}$ )		ROLO08 (0.550 $\mu\text{m}$ )		ROLO10 (0.667 $\mu\text{m}$ )		ROLO12 (0.747 $\mu\text{m}$ )		ROLO14 (0.868 $\mu\text{m}$ )	
	Bias	RMS	Bias	RMS	Bias	RMS	Bias	RMS	Bias	RMS
1. MareS	–2.6	1.6	–3.1	1.2	–2.6	1.4	–2.5	1.6	–2.5	1.7
2. East	9.9	5.6	8.1	4.7	4.9	5.4	5.1	5.1	3.7	5.0
3. North	–31.3	6.2	–33.9	6.5	–33.4	6.3	–32.5	6.7	–28.8	6.6
4. South	–23.8	7.4	–26.9	7.7	–23.7	7.5	–21.4	8.6	–21.8	7.7
5. West	–6.5	4.6	1.0	4.0	–5.0	4.8	–3.4	5.4	–8.0	4.4
6. Aris3	–20.9	6.1	–30.5	4.0	–14.9	5.6	–10.4	6.5	–2.3	5.2
7. Aris7	–18.7	4.1	–22.8	3.2	–12.4	3.6	–8.5	4.6	–2.2	3.3
8. Coper	–6.6	3.2	–11.8	2.8	–8.4	2.9	–6.9	3.6	–4.5	3.0
9. Tycho	–28.9	3.9	–30.6	3.9	–25.9	3.6	–24.6	3.8	–21.0	3.4
10. Highl	–2.4	2.6	–2.8	1.7	–2.3	2.5	–2.7	2.3	–2.9	2.4
11. TyRay	–13.5	2.3	–20.0	1.6	–13.4	2.2	–11.8	2.4	–9.9	2.1

**Table 13**

Bias and RM5 between spectrally-interpolated model predictions with ROLO chip data in VIS–NIR bands based on the ROLO two-regime (maria, highlands) model solution.

Chip	ROLO02 (0.413 $\mu\text{m}$ )		ROLO08 (0.550 $\mu\text{m}$ )		ROLO10 (0.667 $\mu\text{m}$ )		ROLO12 (0.747 $\mu\text{m}$ )		ROLO14 (0.868 $\mu\text{m}$ )	
	Bias	RM5	Bias	RM5	Bias	RM5	Bias	RM5	Bias	RM5
1. Mare5	−4.5	1.5	1.6	1.2	−6.0	1.3	−1.4	1.6	−2.5	1.5
2. East	6.7	5.5	13.1	5.0	2.8	4.8	7.9	5.2	1.6	5.2
3. North	−33.6	5.8	−30.7	6.9	−34.3	6.6	−30.4	6.9	−30.8	6.1
4. South	−26.4	7.0	−23.4	8.0	−24.7	7.8	−18.9	9.0	−24.0	7.2
5. West	−8.9	4.5	5.9	4.4	−7.4	4.7	−1.4	5.6	−9.2	4.3
6. Aris3	−23.3	5.9	−27.1	4.2	−16.6	5.6	−7.9	6.6	−4.4	5.0
7. Aris7	−21.1	3.9	−19.0	3.3	−14.4	3.7	−6.1	4.6	−4.0	3.2
8. Coper	−9.6	2.9	−7.6	3.2	−10.0	3.1	−3.7	3.7	−7.1	2.7
9. Tycho	−31.2	3.6	−27.3	4.2	−27.0	3.9	−22.1	3.9	−23.2	3.0
10. Highl	−5.6	2.4	1.8	1.8	−4.0	2.4	0.6	2.4	−5.5	2.3
11. TyRay	−16.3	2.1	−16.2	1.9	−14.8	2.3	−8.9	2.5	−12.3	1.9

**Table 14**

Bias and RM5 between direct model predictions with ROLO chip data in VIS–NIR bands based on the ROLO three-regime (maria, highland, crater) model solution.

Chip	ROLO02 (0.413 $\mu\text{m}$ )		ROLO08 (0.550 $\mu\text{m}$ )		ROLO10 (0.667 $\mu\text{m}$ )		ROLO12 (0.747 $\mu\text{m}$ )		ROLO14 (0.868 $\mu\text{m}$ )	
	Bias	RM5	Bias	RM5	Bias	RM5	Bias	RM5	Bias	RM5
1. Mare5	−1.2	1.7	−1.7	1.5	1.7	1.6	−1.0	1.7	3.8	2.2
2. East	10.9	6.3	11.1	4.3	9.2	6.3	13.1	5.4	6.9	5.7
3. North	−12.6	6.4	−14.0	7.5	−15.6	6.8	−12.3	7.7	−12.6	7.1
4. South	−14.1	7.3	−15.5	8.7	−12.7	7.7	−6.6	9.9	−13.0	7.8
5. West	−5.2	4.9	3.5	4.3	−0.7	5.5	2.6	6.5	−3.7	4.6
6. Aris3	−14.4	7.4	−23.3	5.7	−5.9	7.1	2.0	8.5	6.2	7.1
7. Aris7	−13.6	4.8	−16.6	4.5	−4.8	4.6	1.8	5.7	5.3	4.5
8. Coper	−2.4	3.4	−5.9	3.5	−1.5	3.7	5.6	5.2	0.6	3.8
9. Tycho	−2.8	5.3	−3.0	4.7	0.1	5.2	3.8	5.8	3.2	5.7
10. Highl	−0.5	2.9	−1.1	2.2	2.9	3.2	8.1	3.3	0.2	2.7
11. TyRay	−6.4	2.7	−11.5	1.9	−4.1	2.6	2.3	3.3	−2.5	2.5

**Table 15**

Bias and RM5 between spectrally-interpolated model predictions with ROLO chip data in VIS–NIR bands based on the ROLO three-regime (maria, highlands, crater) model solution.

Chip	ROLO02 (0.413 $\mu\text{m}$ )		ROLO08 (0.550 $\mu\text{m}$ )		ROLO10 (0.667 $\mu\text{m}$ )		ROLO12 (0.747 $\mu\text{m}$ )		ROLO14 (0.868 $\mu\text{m}$ )	
	Bias	RM5	Bias	RM5	Bias	RM5	Bias	RM5	Bias	RM5
1. Mare5	0.8	1.6	5.5	1.4	−3.6	1.5	0.2	1.8	2.1	1.6
2. East	13.3	7.5	18.2	6.1	6.1	5.1	10.3	5.1	2.5	4.5
3. North	−12.0	5.8	−10.5	7.3	−16.7	7.3	−13.0	7.9	−15.3	7.4
4. South	−13.7	8.0	−11.8	8.9	−14.6	8.8	−9.1	10.3	−16.2	8.8
5. West	−3.2	5.5	10.7	5.1	−4.4	5.1	0.9	5.9	−8.3	4.4
6. Aris3	−12.8	7.4	−18.7	5.6	−8.4	7.2	−0.1	8.4	2.0	6.9
7. Aris7	−11.9	4.7	−11.4	4.3	−7.7	4.6	0.1	5.6	0.8	4.4
8. Coper	0.1	3.5	0.4	2.9	−3.8	3.7	1.8	4.8	−3.4	3.8
9. Tycho	−2.0	5.1	0.7	4.5	−1.1	5.4	3.9	6.0	0.1	5.6
10. Highl	2.1	3.5	8.0	2.7	0.3	2.7	4.0	2.6	−3.8	2.3
11. TyRay	−4.3	3.2	−6.1	1.8	−6.2	2.3	−0.8	2.7	−6.2	2.3

**Table 16**

Bias and RM5 between direct model predictions with ROLO chip data in SWIR bands based on the ROLO three-regime (maria, highland, crater) model solution.

Chip	ROLO54 (1.062 $\mu\text{m}$ )		ROLO57 (1.247 $\mu\text{m}$ )		ROLO58 (1.543 $\mu\text{m}$ )		ROLO60 (1.638 $\mu\text{m}$ )		ROLO62 (1.985 $\mu\text{m}$ )	
	Bias	RM5	Bias	RM5	Bias	RM5	Bias	RM5	Bias	RM5
1. Mare5	0.4	2.9	−9.2	4.0	−3.1	2.7	−3.2	2.2	−4.6	2.2
2. East	11.9	5.3	6.3	10.4	9.1	5.0	7.4	6.5	2.8	4.5
3. North	−14.6	7.0	−10.8	7.5	−5.7	9.1	−9.7	7.3	−11.1	7.7
4. South	−14.2	8.5	−6.7	9.2	−6.4	11.6	−10.4	8.6	−11.8	11.4
5. West	−2.9	5.2	−6.0	6.1	−0.1	5.5	−2.0	5.0	−4.9	4.5
6. Aris3	10.9	5.1	9.1	5.3	12.5	4.9	11.0	4.9	10.2	4.9
7. Aris7	11.0	3.7	8.1	4.0	12.2	3.6	11.0	3.9	10.7	3.8
8. Coper	0.7	3.3	2.7	3.7	2.8	2.8	1.9	3.5	−3.9	3.3
9. Tycho	−0.9	5.0	2.0	5.6	6.0	5.7	2.1	5.5	2.7	5.6
10. Highl	−5.1	2.6	−2.3	2.7	1.6	1.9	−0.6	3.5	−5.4	2.3
11. TyRay	−10.0	2.5	−6.7	3.1	−3.3	2.7	−5.5	3.2	−8.4	2.7



**Table 17**

Bias and RMS between spectrally-interpolated model predictions with ROLO chip data in 5WIR bands based on the ROLO three-regime (maria, highlands, crater) model solution.

Chip	ROLO54 (1.062 $\mu\text{m}$ )		ROLO57 (1.247 $\mu\text{m}$ )		ROLO58 (1.543 $\mu\text{m}$ )		ROLO60 (1.638 $\mu\text{m}$ )		ROLO62 (1.985 $\mu\text{m}$ )	
	Bias	RMS	Bias	RMS	Bias	RMS	Bias	RMS	Bias	RMS
1. Mare5	-1.6	3.0	-1.0	2.6	-5.4	1.9	-4.6	2.2	-3.8	3.0
2. East	11.5	5.3	11.3	10.0	6.4	4.9	7.3	5.3	4.0	6.2
3. North	-11.2	8.1	-7.0	8.4	-9.3	8.1	-8.6	8.1	-11.2	7.0
4. South	-12.3	9.5	-3.2	10.4	-10.1	11.0	-9.4	9.7	-11.8	10.8
5. West	-3.8	5.5	0.0	5.6	-2.5	5.0	-2.4	5.0	-4.1	5.2
6. Aris3	12.0	5.3	14.2	5.4	9.2	4.7	11.2	4.6	11.3	5.3
7. Aris7	11.5	3.8	13.9	4.0	9.1	3.5	10.9	3.6	11.8	4.4
8. Coper	1.4	3.3	5.6	3.7	0.2	2.7	1.5	3.0	-1.9	3.7
9. Tycho	3.3	5.2	6.7	6.0	2.2	5.2	2.9	5.5	2.8	5.5
10. Highl	-4.7	2.4	0.5	2.5	-1.0	2.0	-0.9	2.4	-3.5	3.1
11. TyRay	-8.8	2.5	-3.7	3.1	-6.1	2.5	-5.4	2.7	-7.0	3.1

**Table 18**

Bias and RMS between direct model predictions with ROLO imagery in VIS–NIR bands based on the ROLO three-regime (maria, highland, crater) model solution.

Surface class	ROLO02 (0.413 $\mu\text{m}$ )		ROLO08 (0.550 $\mu\text{m}$ )		ROLO10 (0.667 $\mu\text{m}$ )		ROLO12 (0.747 $\mu\text{m}$ )		ROLO14 (0.868 $\mu\text{m}$ )	
	Bias	RMS	Bias	RMS	Bias	RMS	Bias	RMS	Bias	RMS
Maria	-4.8	4.9	-1.0	4.8	2.4	3.4	3.4	3.6	7.2	3.7
Maria/highlands	-1.4	4.1	2.1	5.0	1.7	3.8	7.0	3.7	5.2	4.5
Highlands	-1.3	2.8	2.7	2.7	-0.9	2.3	6.8	2.5	0.3	2.9
Highlands/crater	-1.4	2.7	3.0	3.0	-1.8	2.2	6.9	2.3	-0.9	2.5
Crater	-1.7	3.3	2.4	2.4	-2.5	2.5	5.0	2.9	0.1	2.5
Overall	-3.2	4.6	0.6	0.6	1.3	3.7	4.9	3.8	5.0	4.8

**Table 19**

Bias and RMS between spectrally-interpolated model predictions with ROLO imagery in VIS–NIR bands based on the ROLO three-regime (maria, highlands, crater) model solution.

Surface class	ROLO02 (0.413 $\mu\text{m}$ )		ROLO08 (0.550 $\mu\text{m}$ )		ROLO10 (0.667 $\mu\text{m}$ )		ROLO12 (0.747 $\mu\text{m}$ )		ROLO14 (0.868 $\mu\text{m}$ )	
	Bias	RMS	Bias	RMS	Bias	RMS	Bias	RMS	Bias	RMS
Maria	-2.1	4.9	4.8	5.0	-1.4	3.4	4.5	3.4	0.7	3.6
Maria/highlands	-0.2	4.1	6.0	5.1	0.3	3.6	6.2	3.7	1.9	4.1
Highlands	-1.3	2.8	5.2	3.4	-0.4	2.3	4.6	2.5	-0.4	2.8
Highlands/crater	-2.1	2.7	4.8	3.7	-0.3	2.2	4.5	2.3	-0.7	2.4
Crater	-3.6	3.4	3.7	4.3	-0.4	2.5	4.7	2.4	-0.2	2.3
Overall	-1.7	4.4	5.0	4.8	-0.8	3.3	4.9	3.3	0.7	3.6

**Table 20**

Bias and RMS between direct model predictions with ROLO imagery in 5WIR bands based on the ROLO three-regime (maria, highlands, crater) model solution.

Surface class	ROLO54 (1.062 $\mu\text{m}$ )		ROLO57 (1.247 $\mu\text{m}$ )		ROLO58 (1.543 $\mu\text{m}$ )		ROLO60 (1.638 $\mu\text{m}$ )		ROLO62 (1.985 $\mu\text{m}$ )	
	Bias	RMS	Bias	RMS	Bias	RMS	Bias	RMS	Bias	RMS
Maria	-0.9	4.2	-13.	3.8	-4.3	3.5	-1.9	3.3	-0.4	3.4
Maria/highlands	-0.9	4.7	-6.2	3.7	0.5	3.5	0.2	3.6	1.3	4.1
Highlands	-5.7	3.0	-5.4	2.8	-0.4	2.9	-3.1	3.0	-2.7	3.0
Highlands/crater	-5.8	2.6	-3.7	2.5	0.5	2.8	-3.4	2.8	-2.9	2.5
Crater	-5.3	2.4	-2.8	2.3	2.5	3.0	-2.0	3.0	-1.0	2.8
Overall	-2.1	4.5	-9.4	5.3	-2.1	4.1	-1.7	3.5	-0.5	3.7

**Table 21**

Bias and RMS between spectrally-interpolated model predictions with ROLO imagery in 5WIR bands based on the ROLO three-regime (maria, highlands, crater) model solution.

Surface class	ROLO54 (1.062 $\mu\text{m}$ )		ROLO57 (1.247 $\mu\text{m}$ )		ROLO58 (1.543 $\mu\text{m}$ )		ROLO60 (1.638 $\mu\text{m}$ )		ROLO62 (1.985 $\mu\text{m}$ )	
	Bias	RMS	Bias	RMS	Bias	RMS	Bias	RMS	Bias	RMS
Maria	-4.7	4.1	-1.4	3.7	-3.3	3.4	-2.6	3.4	-2.5	3.3
Maria/highlands	-2.7	4.5	1.4	4.1	0.0	3.5	0.7	3.6	-0.4	3.9
Highlands	-5.9	3.0	-1.2	2.9	-2.0	2.9	-1.7	2.9	-3.9	3.0
Highlands/crater	-5.2	2.6	-0.6	2.6	-1.8	2.7	-1.5	2.7	-4.1	2.5
Crater	-3.7	2.6	0.9	2.5	-0.5	2.9	-0.2	2.9	-2.4	2.7
Overall	-4.4	4.1	-0.5	3.8	-2.1	3.6	-1.6	3.6	-2.3	3.6

The two-regime (maria, highlands) model was updated by fitting directly to the ROLO data for the “MareS” and “Highl” chips. The comparison of the ROLO observations to the direct model calculations are summarized in Table 12, while Table 13 provides the results for comparison for spectrally-interpolated model predictions. The final model included three regimes (maria, highlands, and crater). For VIS–NIR bands, Table 14 illustrates the comparison of ROLO chip data with model predictions while Table 15 shows the spectrally-interpolated model versus observations. For SWIR bands, Table 16 illustrates the comparison of ROLO chip data with model predictions while Table 17 shows the spectrally-interpolated model versus observations. The last set of tables document the results of comparing the ROLO imagery to the model predictions. Table 18 gives the results based on the direct model calculation and Table 19 gives the results based on the spectrally-interpolated model predictions. Tables 20 and 21 give the performance analysis for the modeled SWIR band imagery. In Tables 18–21, the performance is summarized by surface regime (maria, highland, crater) plus intermediate classes and an “overall” category combining all surface regimes.

## Appendix B. Clementine basemap corrections

While the registration of the Clementine basemap has been significantly improved in the recent release, errors remain related to the absolute calibration of this dataset. In our analysis, we have included the multiplicative correction factor of 0.532 derived by Hillier et al. based on their comparison with past work. However,

in comparing ROLO images near zero phase with the model, we found a striping in the basemap within  $15^\circ$  of the selenographic equator and a systematic East–West linear bias between model and the observations. As described in Section 3.3.1, we attributed this to errors in the basemap that was appropriately corrected.

Besides the striping, other visible artifacts associated with the basemap include: missing data and reduced accuracy near the poles. We have introduced a “cosmetic” correction for the missing data, using the ROLO data as the predictor for the intensity of the basemap. That is, for a given location, we modeled the basemap intensity required to reproduce the observed reflectance. Note that this correction to the basemap is at the  $4''$  resolution of the ROLO data and therefore does not capture the details at the 2-km element size of the Clementine basemap. The process is illustrated in Fig. 18. We have applied this correction in order to generate artifact-free images. However, we have excluded regions associated with missing data in our analysis of the model performance. The accuracy of the model is further impacted near the poles and in a region near the equator where striping is visible. Problems with the calibration of the basemap at the poles are addressed by simply excluding these regions from our analysis. However, a correction for the striping artifact was implemented.

Sharp discontinuities in the image intensity are evident in the basemap. The discontinuities are limited to a band of low selenographic latitudes roughly centered on the equator, between about  $\pm 15^\circ$  latitude. These discontinuities exhibit both a periodicity in the azimuthal direction and a north/south orientation, thereby delineating a series of bands, or “stripes”, as shown in Fig. 19 (left) for an excerpt of the basemap. In surveying Clementine imagery,

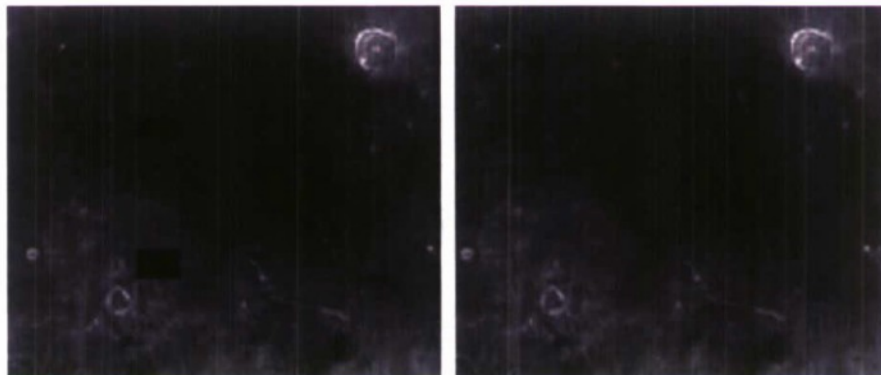


Fig. 18. The hole-filling correction applied to the Clementine basemap. (Left) A portion of the Clementine basemap showing areas with missing data; (right) the resulting basemap after applying the correction.

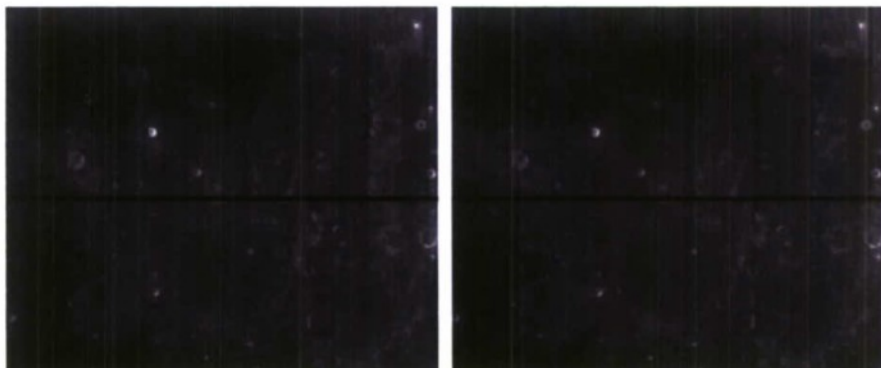


Fig. 19. The striping-correction applied to the Clementine basemap. Left: A portion of the Clementine basemap showing the presence of stripes. Right: Resulting basemap after applying stripe correction algorithm. The dark horizontal line denotes a transect through the image for which the reflectivity is plotted in Fig. 20.



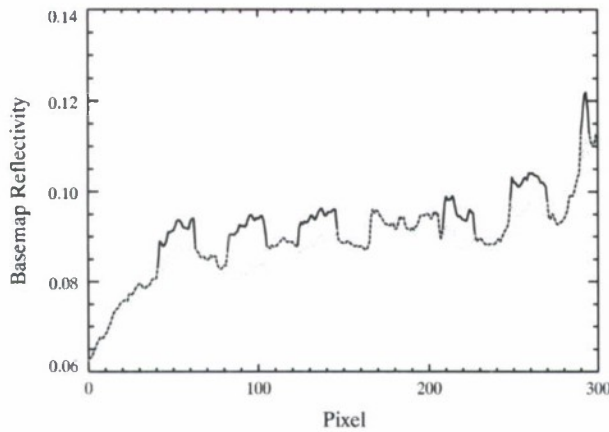


Fig. 20. Reflectivity along the transect shown in Fig. 19. The black line denotes the reflectivity for the original basemap, and the gray dotted line denotes the reflectivity after applying the striping correction algorithm.

we concluded that there are dark offset errors present in the observations and that the stripes consist of alternating positively biased and unbiased stripes.

The stripes are assumed to be an artifact in the surveyed swaths that were normalized the Clementine reflectivity data to a common viewing geometry (i.e.,  $i = 30^\circ$ ,  $e = 0^\circ$ ,  $\alpha = 30^\circ$ ). After normalization, various data swaths were mosaicked together to produce the Clementine basemap image, which exhibits the unintended striping pattern. Since the reflectivity calculations for a location is dependent on the basemap reflectivity (Eq. (17)), striping artifacts present in the basemap would also be present in model calculations. Thus, it is desirable to apply a stripe correction to create a revised basemap with minimum distortion. Using ROLO imagery near zero phase angle as the reference, a three-step correction process was applied.

- (1) Identify all stripe boundaries.
- (2) Identify all stripes that exhibit a reflectivity bias.
- (3) Derive and apply a corrective factor to pixels falling within the biased stripes.

We identify stripe boundaries by applying the Roberts edge detection method (Peli and Malah, 1982) to the basemap image. Since an edge detection algorithm is designed to highlight spatial gradients in two-dimensional imagery, it will be sensitive to both stripe boundaries and naturally occurring edges corresponding to crater ridges and other boundaries between contrasting surface types. To prevent the detection scheme from identifying natural edges, we first smooth the basemap image in the north/south or latitudinal direction (parallel to the stripes). This smoothing preserves the stripe edges while smoothing most naturally occurring edges.

To identify the biased stripes, we perform a search in east/west direction along each row of basemap pixels. The search identifies adjacent edges that bound a local maximum in the basemap reflectivity. As noted above, the striping pattern includes alternating bands of positively biased and unbiased reflectivity. Therefore, the reflectivity correction is applied to these local maximum regions.

For pixels located in biased stripes, the stripe-corrected reflectivity is computed based on the reference ROLO imagery as

$$R_{BM,corr} = R_{BM} - \alpha \frac{R_{ROLO}}{R_{Mod}}$$

where  $R_{Mod}$  is the modeled reflectivity at a pixel location, and  $R_{ROLO}$  is the ROLO-observed reflectivity for the appropriate band. The  $R_{Mod}$

term represents the reflectivity data modeled using the biased basemap, and thus it exhibits the striping artifact. The ROLO data is regridded to the basemap resolution to facilitate this comparison. The  $\alpha$  coefficient is a function of the estimated bias in basemap reflectivity in a stripe region:

$$\alpha = 2 \frac{\sum nPix \Delta R_{Stripe}}{nPix}$$

The  $\Delta R_{Stripe}$  term is the estimated bias for a basemap pixel in a stripe region, and  $nPix$  represents the number of basemap pixels spanning a stripe in the east/west direction. The  $\Delta R_{Stripe}$  term is computed for each pixel as the difference between an estimate of the unbiased reflectivity and the smoothed basemap reflectivity. The unbiased reflectivity estimate is computed by linearly interpolating across the stripe region, using unbiased points outside of the stripe as endpoints. This bias estimate is averaged across the pixels in the stripe region, and then the  $\alpha$  coefficient is tuned by applying an additional scale factor of 2.

The stripe corrected image is shown in Fig. 19 (right). Fig. 20 shows the basemap reflectivity along a transect before and after applying the correction algorithm. The uncorrected reflectivity data clearly shows a periodic striping pattern (solid curve). After correction (dotted curve), the crests in the reflectivity transect are no longer present, while the reflectivity is not altered in the unbiased stripes. Note that for producing this line plot, we smoothed both the uncorrected and corrected data in the north/south direction to damp reflectivity spikes caused by surface roughness, thereby emphasizing reflectivity variations caused by the basemap striping.

## References

- Araki, H., and 10 colleagues, 2009. Lunar global shape and polar topography derived from Kaguya-LALT laser altimetry. *Science* 323, 897–900.
- Archinal, B.A., Rosiek, M.R., Kirk, R.L., Redding, B.L., 2006. The Unified Lunar Control Network 2005, US Geological Survey Open-File Report 2006-1367.
- Buratti, B., Hillier, J., Wang, M., 1996. Lunar opposition surge: Observations by Clementine. *Icarus* 124, 490–499.
- Engelke, C.W., Price, S.D., Kraemer, K.E., 2010. Spectral irradiance calibration in the infrared. XVII. Zero magnitude broadband flux reference for visible to infrared photometry. *Astron. J.*, submitted for publication.
- Folkner, W.M., Williams, J.G., Boggs, D.H., 2008. The Planetary and Lunar Ephemeris DE 421. JPL IOM 343R-08-003.
- Goguen, J.D., Stone, T.C., Kieffer, H.H., Buratti, B.J., 2010. A new look at photometry of the Moon. *Icarus*, in press.
- Hapke, B., 1984. Bidirectional reflectance spectroscopy 3. Corrections for macroscopic roughness. *Icarus* 59, 41–59.
- Hapke, B., 2002. Bidirectional reflectance spectroscopy 5. The coherent backscatter opposition effect and anisotropic scattering. *Icarus* 157, 523–534.
- Hapke, B., 2008. Bidirectional reflectance spectroscopy, 6. Effects of porosity. *Icarus* 195, 918–926.
- Hapke, B.W., Nelson, R.M., Smythe, W.D., 1993. The opposition effect of the Moon – The contribution of coherent backscatter. *Science* 260, 509–511.
- Hartman, B., Domingue, D., 1998. Scattering of light by individual particles and the implications for models of planetary surfaces. *Icarus* 131, 421–448.
- Helfenstein, P., Veverka, J., Hillier, J., 1997. The lunar opposition effect: A test of alternative models. *Icarus* 128, 2–14.
- Helfenstein, P., Shepard, M.K., 1999. Submillimeter scale topography of the lunar regolith. *Icarus* 141, 107–131.
- Hillier, J., Buratti, B., Hill, K., 1999. Multispectral photometry of the Moon and absolute calibration of the Clementine UV/Vis camera. *Icarus* 141, 205–225.
- Kieffer, H.H., Anderson, J.M., 1998. Use of the Moon for spacecraft calibration over 350–2500 nm. *Proc. SPIE* 3948, 325–336.
- Kieffer, H.H., Stone, T.C., 2005. The spectral irradiance of the Moon. *Astron. J.* 129, 2887–2901.
- Kieffer, H.H., Wildey, R.L., 1996. Establishing the Moon as a spectral radiance standard. *Atmos. Ocean. Technol.* 13, 360–375.
- Lawson, S.L., Jakosky, B.M., 2001. Lunar surface thermophysical properties derived from Clementine LWIR and UVVIS images. *J. Geophys. Res.* 106 (E11), 27911–27932.
- Lee, E.M., Gaddis, L.R., Weller, L., Richie, J.O., Becker, T., Shinaman, J., Rosiek, M.R., Archinal, B.A., 2009. A new Clementine Basemap of the Moon. *Lunar Planet. Sci.* 40, XL, 2445.
- Meeus, J., 1991. *Astronomical Algorithms*. William Bell Pub., Richmond, VA.
- Orzin, V.D., 1992. Exact solution for coherent backscattering of polarized light from a random medium of Rayleigh scatterers. *Waves Random Med.* 2, 161–164.

- Nelson, R.M., Hapke, B.W., Smythe, W.D., Spilker, L.J., 2000. The opposition effect in simulated planetary regoliths: Reflectance and circular polarization ratio change at small phase angles. *Icarus* 147, 545–558.
- Peli, T., Malah, D., 1982. A study of edge detection algorithms. *Comput. Graph. Image Process.* 20, 1–21.
- Sasaki, S., Kato, M., Takizawa, Y., 2008. Kaguya (SELENE) science mission. In: *Proceedings on the 26th International Symposium on Space Technology and Science (IST5)*, June 2008, 2008-k-21.
- Shepard, M.K., Helfenstein, P., 2007. A test of the Hapke photometric model. *J. Geophys. Res.* 112, E03001.
- Shorthill, R.W., Saari, J.M., Baird, F.E., LeCompte, J.R., 1969. Photometric Properties of Selected Lunar Features. NASA Contractor Report CR-1429.
- Standish, E.M., 1998. JPL Planetary and Lunar Ephemerides, DE405/LE405, JPL IOM 312.F-98-048.
- Stone, T.C., Kieffer, H.H., 2004. Assessment of uncertainties in ROLO irradiance for on-orbit calibration. *SPIE* 5542, 300–310.
- Stone, T.C., Kieffer, H.H., Anderson, J.M., 2002. Status and use of lunar irradiance for on-orbit calibration. *Proc. SPIE* 4483, 165–175.
- Williams, J.C., Boggs, D.H., Folkner, W.M., 2008. DE421 Lunar Orbit, Physical Librations, and Surface Conditions. JPL IOM 335-JW,D8,WF-20080314-001.